

# Near-infrared chemical abundances of stars in the Sculptor dwarf galaxy

Baitian Tang<sup>1,2\*</sup>, Jiajun Zhang<sup>1,2\*\*</sup>, Zhiqiang Yan<sup>3,4\*\*\*</sup>, Zhiyu Zhang<sup>3,4</sup>, Leticia Carigi<sup>5</sup>, and José G. Fernández-Trincado<sup>6</sup>

<sup>1</sup> School of Physics and Astronomy, Sun Yat-sen University, Zhuhai 519082, China

<sup>2</sup> CSST Science Center for the Guangdong–Hong Kong–Macau Greater Bay Area, Zhuhai, 519082, China

<sup>3</sup> School of Astronomy and Space Science, Nanjing University, Nanjing 210093, China

<sup>4</sup> Key Laboratory of Modern Astronomy and Astrophysics (Nanjing University), Ministry of Education, Nanjing 210093, China

<sup>5</sup> Universidad Nacional Autónoma de México, Instituto de Astronomía, AP 70-264, CDMX 04510, México

<sup>6</sup> Instituto de Astronomía, Universidad Católica del Norte, Av. Angamos 0610, Antofagasta, Chile

Received / Accepted

## ABSTRACT

Owing to the recent identification of major substructures in our Milky Way (MW), the astronomical community has started to reevaluate the importance of dissolved and existing dwarf galaxies. In this work, we investigate up to 13 elements in 43 giant stars of the Sculptor dwarf galaxy (Scl) using high-signal-to-noise-ratio near-infrared (NIR) APOGEE spectra. Thanks to the strong feature lines in the NIR, we were able to determine high-resolution O, Si, and Al abundances for a large group of sample stars for the first time in Scl. By comparing the  $[\alpha/\text{Fe}]$  (i.e., O, Mg, Si, Ca, and Ti) of the stars in Scl, Sagittarius, and the MW, we confirm the general trend that less massive galaxies tend to show lower  $[\alpha/\text{Fe}]$ . The low  $[\text{Al}/\text{Fe}]$  ( $\sim -0.5$ ) in Scl demonstrates the value of this ratio as a discriminator with which to identify stars born in dwarf galaxies (from MW field stars). A chemical-evolution model suggests that Scl has a top-light initial mass function (IMF), with a high-mass IMF power index of  $\sim -2.7$ , and a minimum Type Ia supernovae delay time of  $\sim 100$  Myr. Furthermore, a linear regression analysis indicates a negative radial metallicity gradient and positive radial gradients for  $[\text{Mg}/\text{Fe}]$  and  $[\text{Ca}/\text{Fe}]$ , in qualitative agreement with the outside-in formation scenario.

**Key words.** galaxies: dwarf – stars: abundances – galaxies: evolution

## 1. Introduction

Under the hierarchical galaxy formation scenario, dwarf galaxies are first formed in dark matter subhalos, and later merge to form bigger galaxies, such as our Milky Way (MW). Some of the early mergers can be traced back using their clustering in orbital and kinematical parameter space, and one prominent example is the discovery of Gaia-Sausage-Enceladus (GSE; Belokurov et al. 2018; Helmi et al. 2018), and Sequoia (e.g., Myeong et al. 2019). Some of the more recent minor mergers between dwarf galaxies and the MW created magnificent observable streams; for example the Sagittarius (Sgr) streams (e.g., Majewski et al. 2003; Law & Majewski 2010). Therefore, stars formed in those dissolved and dissolving dwarf galaxies are important building blocks for our MW.

While identifying dissolved dwarf galaxies is painstaking, existing dwarf galaxies are invaluable assets in that they allow us to estimate not only the past but also the future evolution of our Galaxy, as they may be dragged into sufficient proximity by the Galactic potential in the future to merge with our MW. To better chemically tag dissolved dwarf galaxies, a full exploration of the chemistry of existing dwarf galaxies is required. One of the characteristic features of dwarf galaxies is their lower  $[\alpha/\text{Fe}]$  abundances compared to MW disc stars at a given  $[\text{Fe}/\text{H}]$  (Tolstoy et al. 2009). With the help of large spectroscopic surveys, studies

of chemical evolution in dwarf galaxies are more efficient than ever before. Using high-resolution spectra from Apache Point Observatory Galactic Evolution Experiment (APOGEE; Majewski et al. 2017), Hasselquist et al. (2021) explored the chemical abundances of multiple elements (C, N, O, Mg, Al, Si, Ca, Fe, Ni, and Ce) in the Large and Small Magellanic Clouds (LMC and SMC), Sgr dwarf, Fornax dwarf, and GSE. Chemical modeling of  $[\alpha/\text{Fe}]$ – $[\text{Fe}/\text{H}]$  space reveals detailed star-formation epochs, and the possible existence of a second starburst.

The Sculptor (Scl) dwarf galaxy is a particular interesting example. Located at a distance of  $86 \pm 3$  kpc from the Sun (Pietrzyński et al. 2008), with  $M_V = -10.82 \pm 0.14$  mag (Muñoz et al. 2018b), Scl is considered as a textbook dwarf galaxy, with most stars older than 10 Gyr, and is therefore an ideal system with which to empirically investigate chemical evolution (Hill et al. 2019, hereafter H19). As one of the nearby galaxies, Scl can be studied using a resolved color–magnitude diagram (CMD; Weisz et al. 2014). Although much larger samples can be obtained than the spectroscopic ones, estimating the star-formation history from a resolved CMD may suffer from isochrone degeneracy at old ages ( $> 8$  Gyr) and low metallicity. On the other hand, observed chemical abundances combined with proper chemical evolution models (e.g., Vincenzo et al. 2014, de los Reyes et al. 2022) are powerful tools with which to reveal galaxy evolution. Using the medium-resolution spectra ( $R \sim 6500$ ) from DEIMOS (Faber et al. 2003) on the Keck II telescope, C, Mg, Si, Ca, Cr, Mn, Fe, Co, Ni, and Ba abun-

\* email: tangbt@mail.sysu.edu.cn

\*\* email: zhangjj239@mail.sysu.edu.cn

\*\*\* email: yan@nju.edu.cn

dances of Scl stars were investigated in a series of works (Kirby et al. 2010, 2015, 2018; Duggan et al. 2018; de los Reyes et al. 2020). The high-resolution spectra give more accurate chemical abundances, but obtaining these is time consuming. This is why early high-resolution investigations in Scl have small sample sizes (of approximately five stars; e.g., Shetrone et al. 2003; Geisler et al. 2005; Starkenburg et al. 2013; Jablonka et al. 2015; Simon et al. 2015). The Scl sample size is increased to more than 100 in the DART survey (Tolstoy et al. 2006), which used ESO VLT/FLAMES to obtain high-resolution spectra ( $R \sim 20,000$ ) of red giant branch (RGB) stars. In the DART survey, H19 found a marked decrease in  $[\alpha/\text{Fe}]$  over their Scl sample, from the Galactic halo plateau value at low  $[\text{Fe}/\text{H}]$  and then, after a "knee", a decrease to subsolar  $[\alpha/\text{Fe}]$  at high  $[\text{Fe}/\text{H}]$ . The trend was consistent with products of core-collapse supernovae dominating at early times, followed by the onset of supernovae type Ia as early as  $\sim 12$  Gyr ago. By homogeneously analyzing chemical abundances of 380 stars in 13 dwarf galaxies (including Scl), Reichert et al. (2020, hereafter R20) demonstrated that star formation history dominantly depends on galaxy mass.

Despite the wealth of studies on Scl, open key questions remain. For example, (1) it is still not clear as to whether Scl evolves differently in its radial direction. Bettinelli et al. (2019) found that the star formation history of Scl may be different across this dwarf galaxy: star formation in the innermost region was shown to last for longer ( $\sim 1.5$  Gyr) than that in the outermost region ( $\sim 0.5$  Gyr). Given that star formation history can be traced by chemical abundances, we may be able to detect radial gradients of chemical abundances in Scl. Also, Al lines are relatively weak in optical for metal-poor stars, but it is important to discriminate (dissolved) dwarf galaxies from MW field stars (e.g., Das et al. 2020). (2) It would also be helpful to identify a possible trend in Al abundances in Scl. In this work, we plan to tackle these questions by investigating the chemical abundances derived from near-infrared (NIR) APOGEE spectra. The paper is organized as follows. In Section 2, we describe our data and reduction processes. We also present a comparison between our derived elemental abundances and literature values. We compare Scl chemical abundances of O, Mg, Al, Si, Ca, Ti, Cr, Mn, Ni, Ce with those of the MW and other dwarf galaxies in Section 3. To reveal the chemical evolution of Scl behind our observations, we construct its galactic chemical evolution model and discuss its implications. We further discuss radial chemical gradients and N-rich field stars (Section 4). Our final conclusions are outlined in Section 5.

## 2. The Data

### 2.1. Observations and pipeline reduction

Apache Point Observatory Galactic Evolution Experiment (APOGEE, Majewski et al. 2017) was one of the programs operating during the Sloan Digital Sky Survey III (SDSS-III, Eisenstein et al. 2011) and SDSS-IV (Blanton et al. 2017). Multi-object NIR fiber spectrographs observing from both the SDSS 2.5 m telescope at the Apache Point Observatory (Gunn et al. 2006) and the 2.5 m du Pont telescope at the Las Campanas Observatory (Bowen & Vaughan 1973) deliver high-resolution ( $R \sim 22,500$ )  $H$ -band spectra ( $\lambda = 1.51 - 1.69 \mu\text{m}$ ). The APOGEE survey targeted a color-selected sample that predominantly consists of RGB stars across the Milky Way (Zasowski et al. 2017; Santana et al. 2021; Beaton et al. 2021). APOGEE data-reduction software was applied to reduce multiple 3D raw data cubes into calibrated, well-sampled, combined 1D spectra

(Nidever et al. 2015). The stellar parameters were derived using the FERRE code (Allende Prieto et al. 2006), which finds the best solution by comparing the observed spectra with libraries of theoretical spectra (Zamora et al. 2015).

With 17 data releases of SDSS (DR 17; Abdurro'uf et al. 2022) to date, the Scl dwarf galaxy has been observed multiple times, and the signal-to-noise ratios (S/Ns) of stacked spectra has reached a significant level. In this work, we cross-matched the Scl member candidates from Gaia Collaboration et al. (2018) with APOGEE DR17, and 43 stars are selected with  $S/N > 70$ . APOGEE radial velocities (RVs) of these 43 stars are shown to be  $112.4 \pm 8.9$  km/s (Table 1), and all stars are within  $3\sigma$  limits. Therefore, our sample stars are highly likely Scl members based on their locations, proper motions, and RVs. The locations of our sample stars and their positions on a color-magnitude diagram are plotted in Fig. 1. By comparing with previous studies, we find 15 stars in common with H19, and 12 in common with R20. These stars are useful for understanding the systematic errors of our measurements (see below).

### 2.2. Stellar parameters and chemical abundances

In this work, we calculated photometric  $T_{\text{eff}}$  from V band<sup>1</sup> and 2MASS photometry using the prescriptions described in Ramírez & Meléndez (2005). The final  $T_{\text{eff}}$  are the averages of  $T_{\text{eff}}$  derived from dereddened  $(V-J)$ ,  $(V-H)$ ,  $(V-K)$ , where the extinction map is given by Schlegel et al. (1998). Values for  $\log g$  were derived from  $T_{\text{eff}}$ , stellar masses (0.8 solar mass is assumed for all our stars, given the age range of our sample), and bolometric luminosities, where the procedure outlined by Alonso et al. (1999) is used for bolometric correction. Our derived  $T_{\text{eff}}$  and  $\log g$  are shown in Table 1.

Local thermal equilibrium (LTE) chemical abundances (including metallicity from Fe I lines) were analyzed using Brussels Automatic Stellar Parameter (BACCHUS) code (Masseron et al. 2016), where careful line selection and detailed line inspection are performed. The BACCHUS code is developed on top of the radiative transfer code Turbospectrum (Alvarez & Plez 1998; Plez 2012), and model atmosphere is interpolated from MARCS model grids (Gustafsson et al. 2008). To derive chemical abundance for a given absorption line, a sigma-clipping is first applied on the selected continuum points around the targeted line, and then a linear fit is used for the remaining points as the continuum. Therefore, the code can detect significantly poor fits, such as a sudden drop in the spectrum due to bad pixels in the detectors. Observed spectra and model spectra are compared with four different methods to determine abundances: 1)  $\chi^2$  minimization of global goodness-of-fit; 2) core line intensity comparison; 3) equivalent width comparison, and 4) spectral synthesis (see Appendix Fig. in Yu et al. 2021). Furthermore, the code gives each of them a flag to indicate the estimation quality, which is used to reject or accept the line, keeping the best-fit abundance. To increase the credibility of our measurements, we only accept a line when flags indicate the fittings are good in all four methods. If no line meets the above criteria, the abundance is not estimated.

Across the wavelength range of APOGEE spectra, molecular lines of CO, CN, and OH could be significant features affecting the line-by-line abundance analysis. Therefore, we estimated the C, N, O, and Fe abundances self-consistently: we first derived  $^{16}\text{O}$  abundances from  $^{16}\text{OH}$  lines; we then derived  $^{12}\text{C}$  from  $^{12}\text{C}^{16}\text{O}$  lines, and  $^{14}\text{N}$  from  $^{12}\text{C}^{14}\text{N}$ ; and subsequently, iron abundances were derived from Fe I lines. This process was iter-

<sup>1</sup> Coleman et al. (2005), kindly provided by Gary Da Costa.

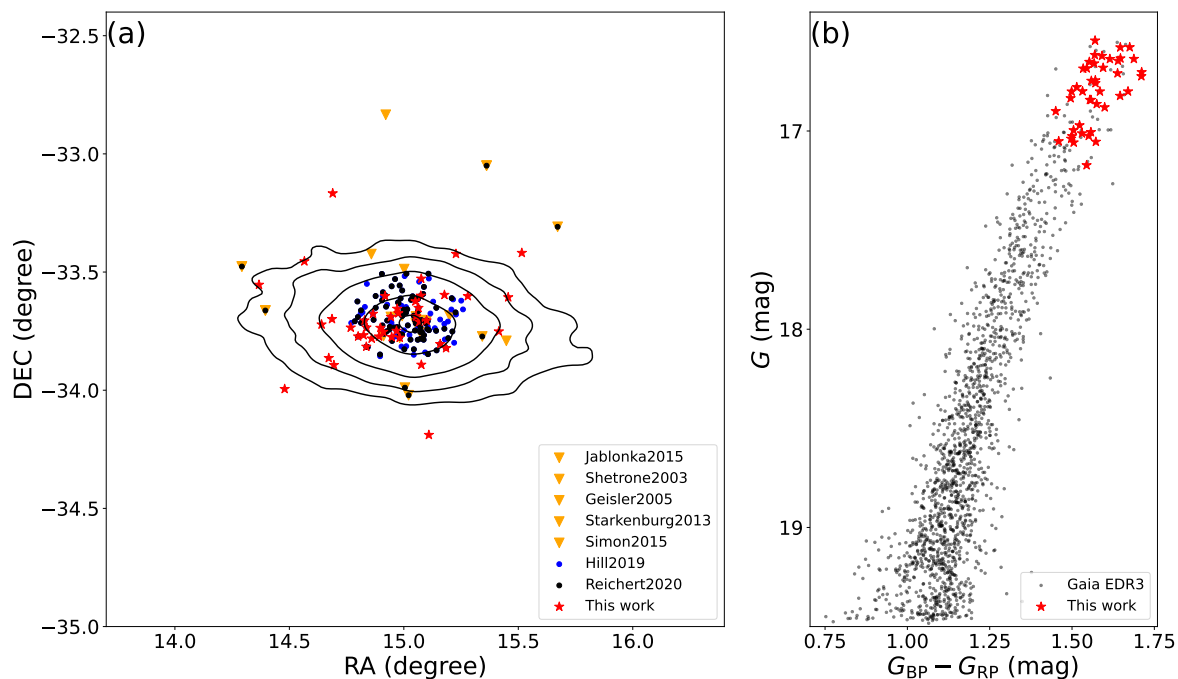


**Fig. 1.** Target information. (a): Spatial distribution of observed Scl stars from the literature. Scl stars from this work are colored red. Blue dots represent stars from H19. Black dots represent stars from R20. Golden triangles show stars from Jablonka et al. (2015), Shetrone et al. (2003), Geisler et al. (2005), Starkenburg et al. (2013), and Simon et al. (2015). An isodensity contour map represented by black lines is plotted based on Table 5 from Muñoz et al. (2018a). (b): Color-magnitude diagram of Scl based on *Gaia* (gray dots).

ated to minimize the dependence of the molecular lines and Fe I lines (Smith et al. 2013). After that, atomic lines of Mg, Al, Si, Ca, Ti, Cr, Mn, Ni, and Ce were analyzed line-by-line. Mg, Al, and Si show strong atomic lines in the observed wavelength, and therefore the abundances of these elements are mostly complete across our sample stars. On the other hand, a large number of Cr, Mn, Ni, and Ce atomic lines and  $^{12}\text{C}^{16}\text{O}$  and  $^{12}\text{C}^{14}\text{N}$  molecular lines are too weak to give meaningful results; these were therefore rejected visually to avoid false detection. The derived chemical abundances of our targets are given in Table 2. We assumed solar abundances of Asplund et al. (2005) in this work. Other chemical elements mostly show weak atomic features in the observed wavelength (e.g., Na), which is partially because of the metal-poor nature of our stars ( $[\text{Fe}/\text{H}] < -1$ ), and these are not discussed here.

We analyzed the internal errors by propagating typical errors in  $T_{\text{eff}}$ ,  $\log g$ , and  $[\text{Fe}/\text{H}]$ . The typical errors are set as  $\Delta T_{\text{eff}} = 100$  K,  $\Delta \log g = 0.25$  dex, and  $\Delta[\text{Fe}/\text{H}] = 0.1$  dex. The total estimated error is therefore calculated as:  $\sigma_{\text{tot}} = ((\sigma_{\Delta T_{\text{eff}}})^2 + (\sigma_{\Delta \log g})^2 + (\sigma_{\Delta[\text{Fe}/\text{H}]})^2)^{1/2}$ . The abundance errors of a typical star (#21) are shown in Table 3 as an example.

### 2.3. Comparison with literature

As our study is the first to investigate Scl chemical abundances in NIR, it is important to investigate the possible systematic errors associated with our approach by comparing our results with those obtained from optical spectra. The upper panels of Fig. 2 show a comparison of the stellar parameters  $T_{\text{eff}}$ ,  $\log g$ , and

$[\text{Fe}/\text{H}]$  from our work with those derived from optical spectra in the literature. Given that H19 adopted photometric  $T_{\text{eff}}$ , and R20 adopted spectroscopic  $T_{\text{eff}}$ , our  $T_{\text{eff}}$  agree better with those of H19, but there is still an offset ( $\sim 100$  K). In H19,  $T_{\text{eff}}$  were derived by averaging over  $T_{\text{eff}}$  from  $(V-I)$ ,  $(V-J)$ ,  $(V-K)$ , where  $T_{\text{eff}}$  determined from  $(V-I)$  are on average 200 K hotter than those from  $(V-J)$  and  $(V-K)$ . As most of our sample stars are outside the application range of the  $(V-I) - T_{\text{eff}}$  relation, we chose not to use  $T_{\text{eff}}$  determined from  $(V-I)$ , and therefore our adopted  $T_{\text{eff}}$  are cooler than those of H19. Interestingly, our adopted  $T_{\text{eff}}$  show no significant systematic offset compared to the uncalibrated ASPCAP  $T_{\text{eff}}$ , with a small difference scatter ( $\sim 25$  K). The  $\log g$  from our work are generally smaller than those of R20, which is related to the cooler  $T_{\text{eff}}$  that we adopted. However, our  $\log g$  are larger than those derived in H19, which may be a result of adopting spectroscopic  $\log g$  in H19.  $[\text{Fe}/\text{H}]$  derived in this work is consistent with that of H19, while being slightly more metal poor than that of R20, which is related to the cooler  $T_{\text{eff}}$  and smaller  $\log g$  in this work.

We compare the element abundances that we find here with those from other optical studies in Fig. 2. For  $[\text{O}/\text{H}]$ ,  $[\text{Si}/\text{H}]$ ,  $[\text{Ca}/\text{H}]$ , and  $[\text{Ni}/\text{H}]$ , most of the data points are located on both sides of the 1:1 line, although with large scatter or low number statistics. For example, O and Si are measured in all our sample stars, but they were only measured in a small portion of the star sample of H19, and none were measured in R20. This is due to the stronger OH molecular lines and Si atomic lines in the NIR. However, the opposite is true for Ni. The large scatter in Ti is caused by the large derivation uncertain-

**Table 1.** Basic information on our sample stars

#	APOGEE_ID	RA (deg)	DEC (deg)	$T_{\text{eff}}$ (K)	$\log g$	$RV$ (km s <sup>-1</sup> )	S/N	Vmag (mag)	Kmag (mag)	Common stars
1	2M00572816-3333133	14.36736	-33.55371	4134.40	0.54	130.14	78.26	17.10	13.94	
2	2M00575508-3359410	14.47952	-33.99473	4154.82	0.58	109.23	96.70	17.15	13.99	
3	2M00581573-3327163	14.56557	-33.45455	4081.40	0.53	125.84	96.36	17.16	13.97	
4	2M00583377-3343187	14.64074	-33.72189	4140.10	0.70	108.88	74.05	17.47	14.32	
5	2M00584131-3351495	14.67213	-33.86376	4112.41	0.54	120.51	104.48	17.13	13.95	
6	2M00584470-3341561	14.68628	-33.69893	4062.10	0.50	118.97	107.77	17.11	13.81	
7	2M00584546-3310006	14.68944	-33.16685	4023.17	0.50	118.33	85.75	17.15	13.79	
8	2M00584671-3353367	14.69464	-33.89354	4246.87	0.80	140.39	71.75	17.54	14.63	
9	2M00590432-3344058	14.76802	-33.73496	4173.28	0.73	110.49	77.67	17.49	14.46	
10	2M00591209-3346208	14.80041	-33.77246	4253.53	0.72	111.52	80.36	17.32	14.43	R20, H19
11	2M00591778-3346016	14.82411	-33.76712	4139.96	0.69	108.16	80.87	17.47	14.32	
12	2M00591884-3342175	14.82854	-33.70488	4084.08	0.71	117.61	71.03	17.63	14.49	R20, H19
13	2M00592065-3348566	14.83607	-33.81574	4063.73	0.50	112.98	116.24	17.13	13.86	R20, H19
14	2M00592081-3344049	14.83672	-33.73470	4229.56	0.68	109.23	91.78	17.25	14.36	R20, H19
15	2M00592626-3346529	14.85945	-33.78136	4096.45	0.56	94.81	98.34	17.22	14.01	
16	2M00592768-3340356	14.86537	-33.67656	4146.20	0.58	119.66	94.59	17.17	14.03	H19
17	2M00593400-3346210	14.89168	-33.77252	4139.87	0.71	107.25	74.42	17.51	14.34	
18	2M00593538-3344094	14.89743	-33.73597	3841.07	0.34	111.25	115.04	17.31	13.62	
19	2M00593841-3345107	14.91005	-33.75299	4091.02	0.68	116.77	77.19	17.52	14.24	
20	2M00594032-3336064	14.91802	-33.60178	4095.91	0.68	112.45	75.22	17.53	14.49	
21	2M00594641-3341233	14.94341	-33.68982	3908.62	0.39	107.26	110.67	17.25	13.75	H19, Geisler2005
22	2M00594727-3346305	14.94696	-33.77516	4029.68	0.63	106.54	80.78	17.54	14.25	
23	2M00595228-3344546	14.96784	-33.74850	4105.40	0.61	117.41	94.57	17.32	14.07	H19
24	2M00595302-3339189	14.97092	-33.65527	3964.64	0.51	111.28	89.88	17.40	14.01	
25	2M00595422-3340270	14.97593	-33.67418	4068.80	0.65	99.17	77.54	17.51	14.36	R20, H19
26	2M00595568-3346400	14.98202	-33.77778	4182.28	0.65	121.84	83.97	17.28	14.25	R20, H19, Geisler2005
27	2M01001215-3337260	15.05064	-33.62389	4107.19	0.50	113.06	109.85	17.01	13.81	
28	2M01001278-3341157	15.05328	-33.68772	4197.29	0.66	97.31	78.73	17.26	14.30	R20, H19, Shetrone2003
29	2M01001537-3339060	15.06407	-33.65169	4071.09	0.58	112.78	88.81	17.33	14.20	R20, H19
30	2M01001630-3342371	15.06795	-33.71033	3959.43	0.38	103.56	110.03	17.07	13.70	Geisler2005
31	2M01001777-3335597	15.07408	-33.59993	3968.14	0.49	120.20	93.51	17.34	13.95	R20, H19
32	2M01001821-3331405	15.07590	-33.52794	3978.96	0.54	105.27	95.09	17.41	13.93	
33	2M01001833-3353314	15.07641	-33.89208	4112.65	0.62	128.62	81.15	17.34	14.14	
34	2M01002384-3342173	15.09937	-33.70483	4073.31	0.58	122.14	77.80	17.33	14.05	R20, H19, Geisler2005
35	2M01002624-3411206	15.10937	-34.18906	4076.53	0.60	122.50	87.82	17.36	14.09	
36	2M01003813-3348168	15.15889	-33.80468	4071.18	0.55	107.07	89.94	17.25	13.92	R20, H19
37	2M01004256-3335475	15.17736	-33.59654	4139.44	0.55	113.03	96.69	17.10	13.98	
38	2M01004427-3349188	15.18449	-33.82190	4053.48	0.64	112.67	71.51	17.52	14.32	R20, H19
39	2M01005465-3325231	15.22775	-33.42311	4036.26	0.56	104.17	86.07	17.36	14.06	
40	2M01010709-3336065	15.27957	-33.60181	4049.61	0.52	107.91	90.37	17.23	14.01	
41	2M01013961-3345043	15.41507	-33.75120	3993.39	0.45	103.55	95.28	17.16	13.78	
42	2M01014939-3336241	15.45583	-33.60670	4003.54	0.50	113.29	93.68	17.17	13.87	
43	2M01020368-3325079	15.51535	-33.41888	4091.18	0.55	99.55	82.42	17.21	13.94	

Note: R20-Reichert et al. (2020), H19-Hill et al. (2019), Geisler2005-Geisler et al. (2005), Shetrone2003-Shetrone et al. (2003).

ties (see Table 3) due to the relative weakness of the atomic lines in APOGEE spectra. For Mg, we find an under-abundance of  $\sim 0.4$  dex compared to the literature. The nonLTE (NLTE) corrections for optical Mg lines are relatively small in the metallicity range that we are interested in ( $-2 < [\text{Fe}/\text{H}] < -1$ ; see Fig. 6 of R20). Meanwhile, according to NLTE investigations of Mg lines in the APOGEE wavelengths (e.g., Zhang et al. 2017; Osorio et al. 2020; Lind et al. 2022), the NLTE correction for Mg could be negligible when the spectral resolution is sufficiently high ( $R \sim 100,000$ ). However, lower resolution spectra may not resolve the cores of the lines adequately, resulting in a substantial NLTE correction (0.2–0.4 dex) for the prominent Mg triplet ( $\lambda \sim 15741, 15749, 15766 \text{ \AA}$ ) in the APOGEE spectra (Osorio et al. 2020; Masseron et al. 2021). The Mg abundances in this work are in good agreement with those from the APOGEE DR17 pipeline. The aforementioned Mg under-abundance should be common for metal-poor giant stars when comparing APOGEE-derived abundances with optical ones. The comparison here reveals a caveat that must be taken into account when interpreting our results.

## 3. Results

### 3.1. $\alpha$ -elements

The  $\alpha$ -elements are mainly generated in massive stars through type II supernovae (SNe II), and consequently their recycle timescale in the interstellar medium is much smaller than that of iron, which is mainly produced in type Ia SNe (SNe Ia). As a result, the  $[\alpha/\text{Fe}]$  abundance is initially enhanced, and starts to decline with  $[\text{Fe}/\text{H}]$  after the SNe Ia delay time (Matteucci & Greggio 1986). The declining point, or the “knee” in  $[\alpha/\text{Fe}]$  versus  $[\text{Fe}/\text{H}]$  trend, is related to the star formation rate and therefore galaxy mass: the less massive the galaxy, the more metal-poor the  $[\alpha/\text{Fe}]$  turnover.

The  $[\alpha/\text{Fe}]$ - $[\text{Fe}/\text{H}]$  relations are shown in Fig. 3. In the background, we also include MW halo, disc, and dwarf galaxy stars<sup>2</sup>.  $[\alpha/\text{Fe}]$  of our sample stars all show declining trends as a function of metallicity. We note that (1) this is the first time that high-resolution O and Si abundances have been investigated with such

<sup>2</sup> To maintain the legibility of each figure, but still grasp the essence of abundance changes with respect to galaxy mass, we only select the two most representative and well-studied examples: MW and Sgr. For chemical abundances of other nearby dwarf galaxies, please refer to R20 or Hasselquist et al. (2021).

**Table 2.** Chemical abundances

#	[Fe/H]	[C/Fe]	[N/Fe]	[O/Fe]	[Mg/Fe]	[Al/Fe]	[Si/Fe]	[Ca/Fe]	[Ti/Fe]	[Cr/Fe]	[Mn/Fe]	[Ni/Fe]	[Ce/Fe]
1	-1.75	...	...	0.34	-0.01	...	0.07	...	...	...	...	...	...
2	-2.16	...	...	0.25	0.30	-0.55	0.35	0.61	...	...	...	...	...
3	-1.91	...	...	0.31	0.05	-0.38	0.22	0.48	...	...	...	...	...
4	-1.92	...	...	0.67	0.12	-0.55	0.22	0.66	...	...	...	...	...
5	-2.01	...	...	0.23	-0.15	-0.55	0.22	0.47	...	...	...	...	...
6	-2.13	...	...	0.21	0.14	-0.52	0.19	...	...	...	...	...	...
7	-1.64	0.40	0.86	0.34	-0.02	-0.69	0.08	...	...	...	...	...	0.64
8	-1.81	...	...	0.31	0.08	-0.24	0.13	...	...	...	...	...	...
9	-1.60	...	...	0.23	...	-0.67	0.04	-0.01	-0.13	...	...	...	...
10	-1.88	0.57	1.42	0.75	...	-0.46	0.13	...	...	...	...	...	...
11	-1.59	...	...	0.19	-0.31	-0.63	0.05	0.26	...	...	...	...	...
12	-1.22	...	...	0.05	-0.57	...	0.03	-0.12	-0.47	...	...	...	...
13	-1.76	...	...	0.32	0.05	-0.44	0.22	0.34	0.16	...	...	...	...
14	-1.91	...	...	0.35	-0.28	-0.67	0.09	...	...	...	...	...	...
15	-1.94	-0.17	...	0.25	-0.03	-0.63	0.11	0.05	...	...	...	...	...
16	-2.09	...	...	0.23	0.08	-0.58	0.20	0.12	...	...	...	...	...
17	-1.61	...	...	0.34	-0.02	...	0.18	0.43	...	...	...	...	...
18	-1.05	-1.10	...	-0.21	-0.44	-1.10	-0.03	-0.31	-0.70	-0.22	-0.47	...	-0.33
19	-1.59	...	...	0.08	-0.07	-0.41	0.18	0.17	...	...	...	0.16	...
20	-1.57	...	...	0.21	-0.03	-0.68	0.09	0.24	0.40	...	...	0.18	...
21	-1.05	-0.58	...	-0.00	-0.36	-0.94	-0.03	-0.07	-0.62	0.03	-0.29	-0.38	-0.25
22	-1.15	-0.63	...	-0.02	-0.31	-1.06	-0.03	-0.15	0.16	...	-0.41	...	-0.24
23	-2.05	...	...	0.29	0.04	-0.55	0.19	-0.09	...	...	...	...	...
24	-1.14	-1.16	...	-0.10	-0.48	-0.88	-0.00	-0.08	...	0.12	-0.21	...	...
25	-1.30	-0.52	...	0.10	...	-0.34	-0.04	0.07	0.29	...	-0.11	...	...
26	-2.14	...	...	0.32	0.02	-0.60	0.13	...	...	...	...	...	...
27	-1.65	...	...	0.38	-0.06	-0.49	0.16	0.15	0.14	...	...	...	0.19
28	-1.73	-0.12	...	0.30	-0.06	-0.63	0.05	...	...	...	...	...	...
29	-1.42	...	...	0.05	-0.10	...	0.16	...	...	...	...	-0.08	...
30	-1.43	0.40	1.61	0.37	...	-0.69	0.17	...	-0.28	...	...	...	2.23
31	-1.13	-0.76	...	-0.05	...	-1.18	0.02	-0.04	-0.33	-0.03	-0.32	...	-0.23
32	-1.63	...	...	0.32	0.11	-0.50	0.31	...	...	...	...	0.26	...
33	-1.72	...	...	0.33	-0.10	-0.53	0.15	...	-0.08	...	...	...	...
34	-1.71	...	...	0.14	-0.11	-0.42	0.30	...	-0.22	...	...	...	...
35	-1.86	...	...	0.19	0.11	-0.26	0.16	-0.04	...	...	...	...	...
36	-1.76	...	...	0.20	0.03	-0.33	0.16	-0.03	...	...	...	...	...
37	-1.81	...	...	0.33	-0.06	...	0.06	...	...	...	...	...	...
38	-1.32	...	...	-0.01	...	-0.50	0.11	0.26	0.35	...	...	-0.46	...
39	-1.55	...	...	0.21	-0.06	-0.53	0.19	0.09	...	...	...	...	...
40	-1.57	-0.10	...	0.06	...	...	-0.08	-0.03	...	...	...	...	...
41	-1.56	...	...	0.17	-0.04	-0.50	0.15	0.10	...	...	...	0.10	0.00
42	-1.33	-0.80	...	0.03	...	-1.00	0.03	0.05	-0.53	-0.44	...	...	-0.08
43	-2.05	...	...	0.16	0.04	-0.49	0.24	0.45	0.68	...	...	...	...

**Table 3.** Errors of chemical abundances propagated from atmospheric parameters for star #21

Element	$\Delta T_{\text{eff}} = 100$ (K)	$\Delta \log(g) = 0.25$ (dex)	$\Delta[\text{Fe}/\text{H}] = 0.1$ (dex)	$\sigma_{\text{tot}}$
[Fe/H]	0.022	0.171	0.012	0.173
[C/Fe]	0.272	0.515	0.250	0.634
[N/Fe]	...	...	...	...
[O/Fe]	0.237	0.080	0.002	0.250
[Mg/Fe]	...	0.185	...	...
[Al/Fe]	0.080	0.046	0.010	0.093
[Si/Fe]	0.002	0.011	0.012	0.016
[Ca/Fe]	0.049	0.177	0.015	0.185
[Ti/Fe]	1.010	0.053	0.883	1.343
[Cr/Fe]	0.111	0.201	0.018	0.230
[Mn/Fe]	0.007	0.112	0.020	0.114
[Ni/Fe]	0.002	0.018	0.043	0.047
[Ce/Fe]	0.040	0.027	0.024	0.053

a large sample size in Scl, which is thanks to their strong feature lines in the NIR; and that (2) Ti lines in the observed spectra are relatively weak, especially for more metal-poor stars. As a result, our Ti abundances show larger scatter than those of H19 and R20.

In terms of galaxy mass, the MW is much larger than Sgr and Scl, and we confirm that MW stars show the largest  $[\alpha/\text{Fe}]$  element abundances among them. Comparing  $[\alpha/\text{Fe}]$  of our study and those of Sgr, where similar NIR lines were used to derive abundances, we find that Scl stars of this work show systemat-

ically lower  $[\alpha/\text{Fe}]$  than Sgr stars, particularly at  $[\text{Fe}/\text{H}] > -1.5$ . This is more robust for O, Mg, and Si, but is less evident for Ca and Ti. Our observations qualitatively agree with the theory that less massive galaxies generate less  $\alpha$  elements.

### 3.2. Al

Al is mainly synthesized by C and Ne burning in massive stars (Arnett 1971; Woosley & Weaver 1995), but can also be modified by the Mg-Al cycle activated at higher core temperatures

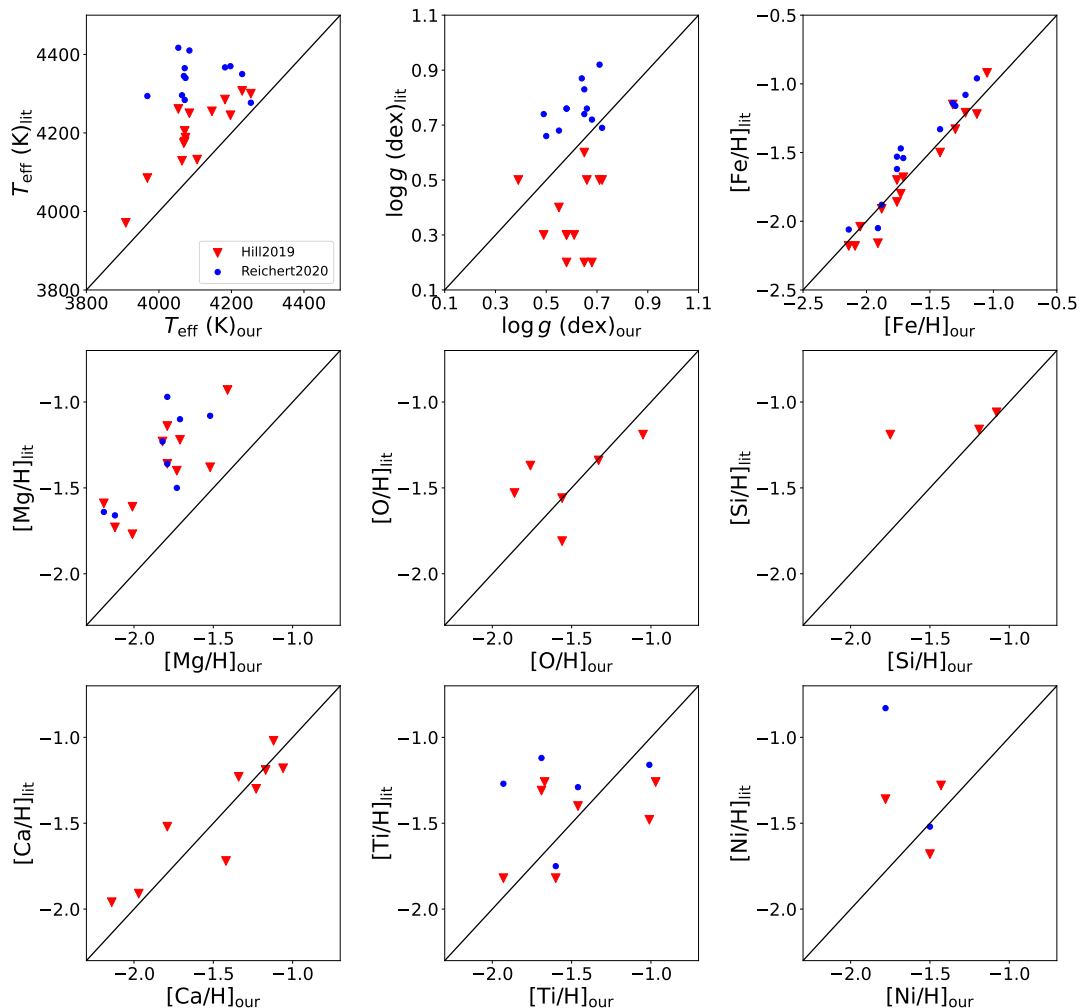


**Fig. 2.** Comparison of stellar atmospheric parameters and elemental abundances of this work with those from the literature. Our results and those from the literature are denoted “our” and “lit”, respectively. Red triangles represent comparisons between our work and H19 and blue circles represent comparisons between our work and R20. The black solid line is the 1:1 relation.

during the asymptotic giant branch (AGB) H-burning phase (Arnould et al. 1999). However, the nonexistence of a Mg-Al anti-correlation and the small scatter of  $[\text{Mg}/\text{Fe}]$  at a given metallicity suggest that the Mg-Al nucleosynthesis cycle does not significantly change their abundances; that is, the Al abundances of our sample reflect their primordial chemistry.

In this work, we determine Al abundances of a large group of Scl stars for the first time. There is a concern that NLTE correction for Al could be substantial ( $\sim 0.4$  dex) for very metal-poor stars ( $[\text{Fe}/\text{H}] < -2.0$ ) when using optical lines (Andrievsky et al. 2008; Mashonkina et al. 2017). However, Lind et al. (2022) suggested that the NLTE correction for Al lines in the APOGEE spectral range ( $\lambda \sim 16719, 16751, 16763 \text{ \AA}$ ) is negligible ( $< 0.1$  dex).  $[\text{Al}/\text{Fe}]$  of Scl stars show a decreasing trend as the metallicity increases. This is expected considering that Al is mainly synthesized in massive stars. Compared to the majority of MW

field stars,  $[\text{Al}/\text{Fe}]$  of dwarf galaxies (Scl and Sgr) are systematically lower (Fig. 4, upper panel). The deficient  $[\text{Al}/\text{Fe}]$  in Sgr was pointed out by Hasselquist et al. (2017). Given the similar nucleosynthetic origins of Al and Mg, their ratio could be informative. In terms of  $[\text{Al}/\text{Mg}]$  (Fig. 4, lower panel), Scl stars show a flat trend as a function of metallicity, while Sgr and MW stars show clear increasing trends. This trend reflects the increasing yield of Al over  $\alpha$ -elements with initial stellar metallicity. There are also a group of halo field stars with  $[\text{Fe}/\text{H}] < -2.5$  showing  $[\text{Al}/\text{Fe}] \sim -0.7$  and  $[\text{Al}/\text{Mg}] \sim -1.0$ . It has been suggested that these stars originate from dissolved dwarf galaxies (e.g., Das et al. 2020). Al is an excellent tracer with which to chemically tag stars of extragalactic origin.

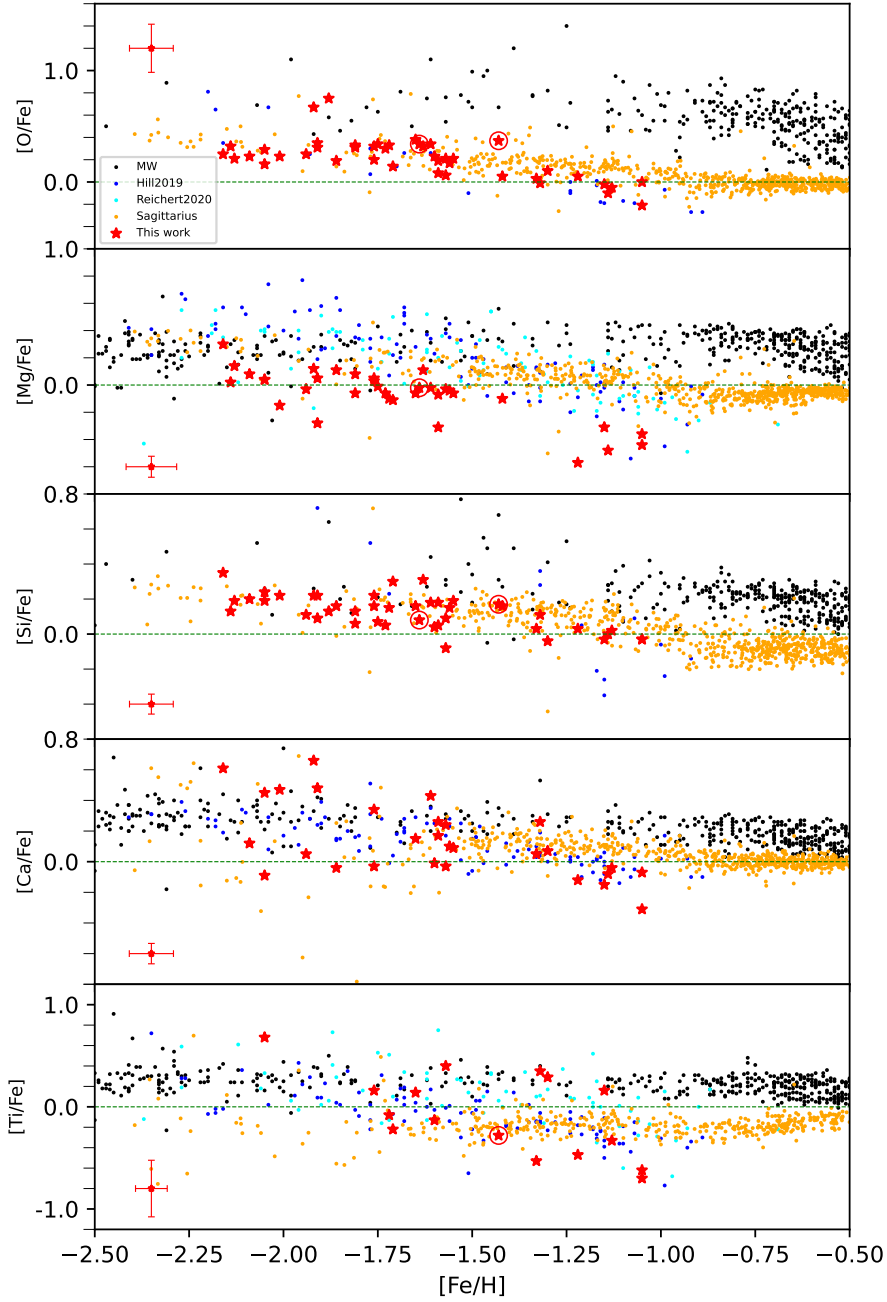


**Fig. 3.**  $[\alpha/\text{Fe}]$  vs.  $[\text{Fe}/\text{H}]$ . Scl stars from this work are labeled as red stars. The error bar in each panel indicates the median uncertainty of available measurements. Possible AGB stars are outlined with large circles. Black dots correspond to MW stars from the halo (92 out of 168 stars from Fulbright 2000, 35 stars from Cayrel et al. 2004, 234 out of 253 stars from Barklem et al. 2005, 131 out of 199 stars from Yong et al. 2013, 287 out of 313 stars from Roederer et al. 2014), and MW stars from the disc (174 out of 181 stars from Reddy et al. 2003, 153 out of 176 stars from Reddy et al. 2006, 679 out of 714 stars from Bensby et al. 2014). Blue and cyan dots represent Scl stars from H19 and R20, respectively. Orange dots represent Sgr stars from Hasselquist et al. (2021).

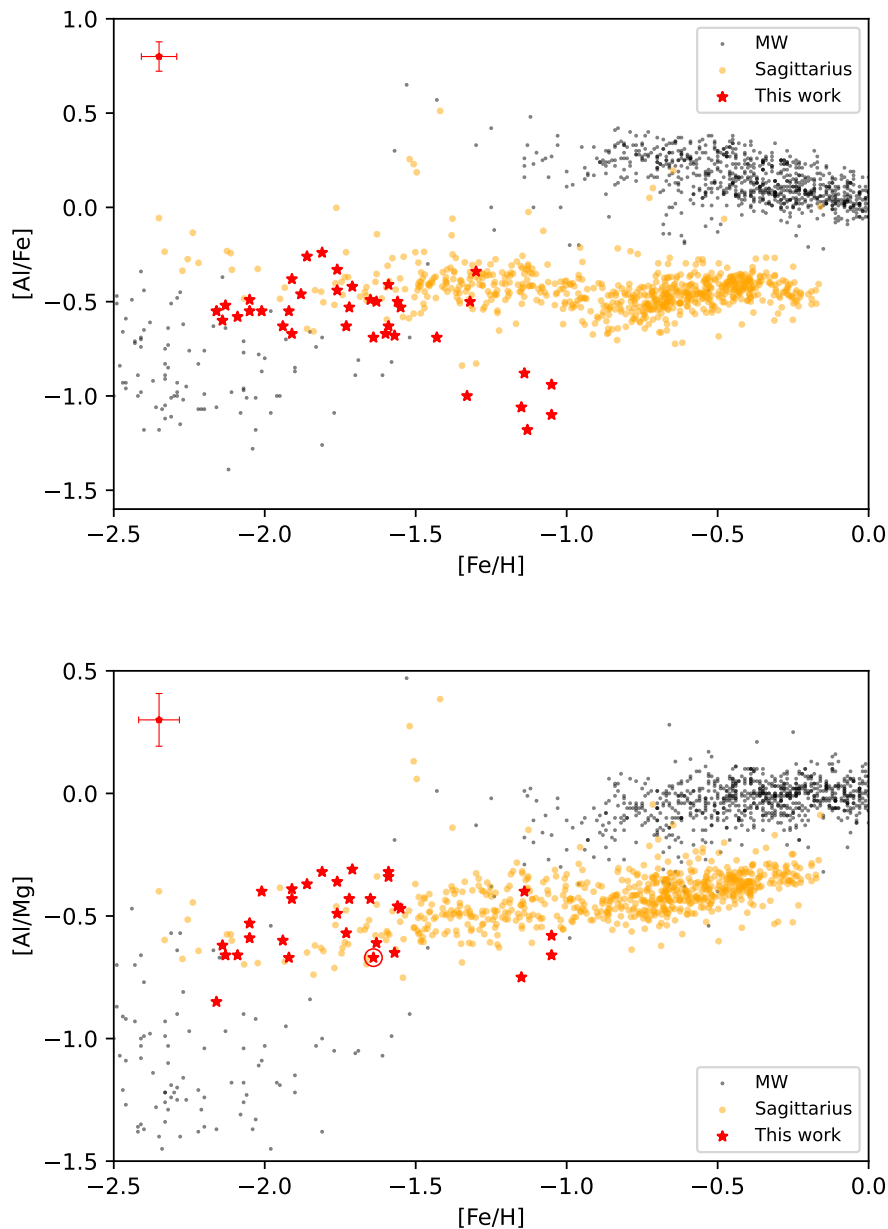


**Fig. 4.**  $[\text{Al}/\text{Fe}]$  ( $[\text{Al}/\text{Mg}]$ ) vs.  $[\text{Fe}/\text{H}]$  relations. Symbols are the same as in Fig. 3.

### 3.3. Iron-peak elements

Though SNe Ia runaway deflagration obliterations of white dwarfs have a signature more tilted towards the iron-peak group (Nomoto et al. 1997), the solar composition of the iron-peak elements are in fact a heterogeneous combination of both SNe Ia and core-collapse SNe II (Woosley & Weaver 1995). As dwarf galaxies and MW have different star-formation timescales, this discrepancy may manifest itself in iron-peak elements.

As the iron-peak elements investigated in this study show weak atomic lines in the observed spectra, only a few measurements are available, mostly for more metal-rich stars. The upper panel of Fig. 5 shows that our  $[\text{Cr}/\text{Fe}]$  abundances are generally consistent with those of H19 and R20 in a similar metallicity range. Similar conclusions can be drawn for  $[\text{Mn}/\text{Fe}]$ . As our measurements of Cr and Mn are concentrated in a small metal-

licity range, to avoid over-interpreting our data, we refer to the aforementioned studies for their astrophysical implications.

Albeit based on a small sample size,  $[\text{Ni}/\text{Fe}]$  shows a seemingly decreasing trend as a function of  $[\text{Fe}/\text{H}]$ , which is similar to other  $\alpha$ -elements. This is consistent with the Ni trend observed by H19, who suggested this could be a result of the low contribution of Ni from SNe Ia (also see Nissen & Schuster 2011). However, the decreasing trend of Ni in R20 is less evident, indicating a more dedicated investigation of Ni is necessary.

### 3.4. Neutron-capture elements

Elements heavier than iron are mostly generated via neutron-capture processes. Depending on the relative speed of neutron capture compared to  $\beta$ -decay, the neutron-capture processes are divided into two types, rapid ( $r$ -) and slow ( $s$ -). The astrophysi-



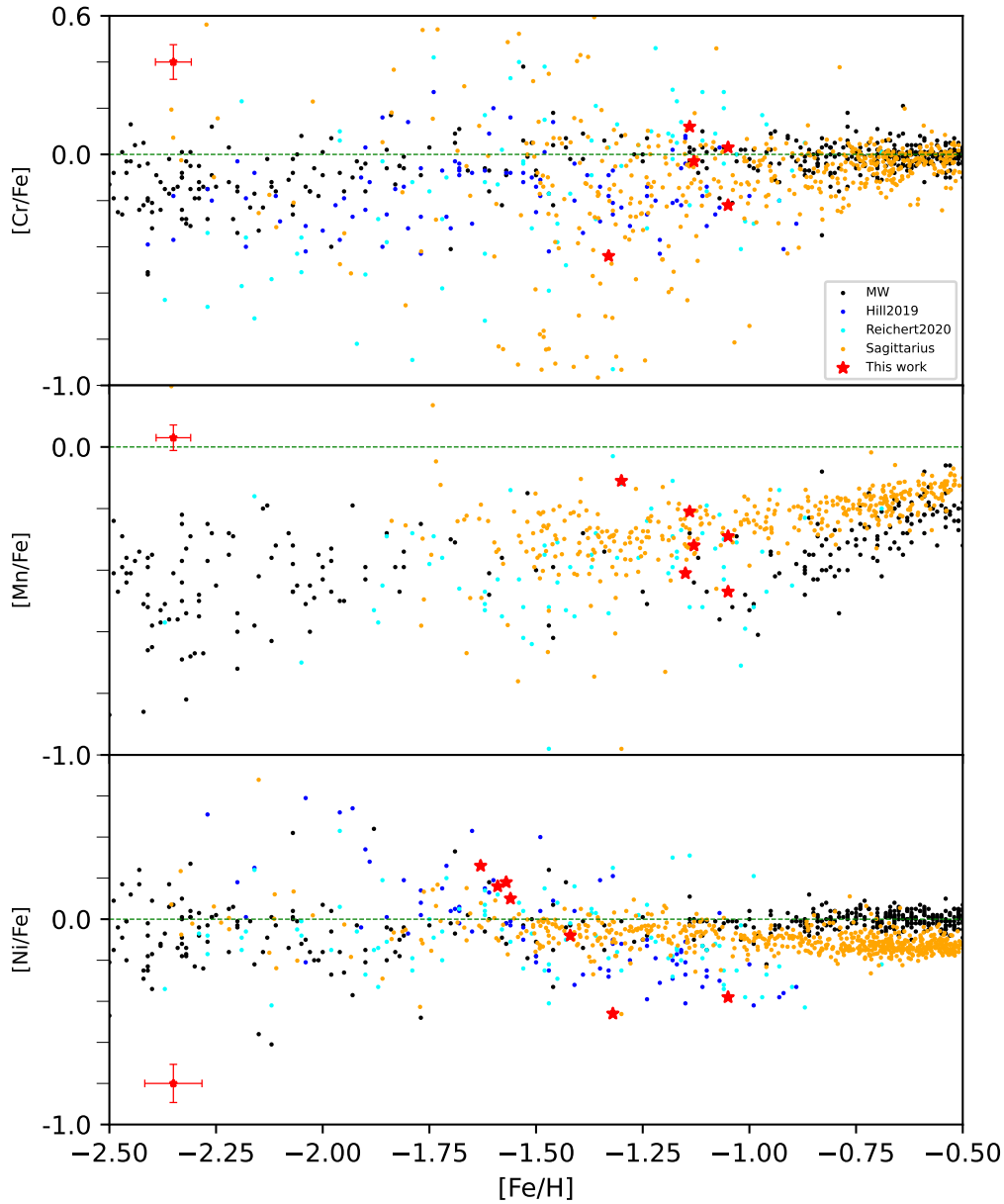


**Fig. 5.** Abundances of iron peak elements vs.  $[\text{Fe}/\text{H}]$ . Symbols are the same as in Fig. 3.

cal sites of  $r$ -process element production have been debated over the past 60 years (e.g., Thielemann et al. 2011; Kajino et al. 2019). The more popular models include core collapse SNe (e.g., Woosley et al. 1994) and neutron star mergers (e.g., Côté et al. 2018; Watson et al. 2019). The main  $s$ -process elements are synthesized by AGB stars during thermal pulsations (Busso et al. 2001; Karakas & Lattanzio 2014). Two nuclear reactions are the major neutron excess sources in AGB stars:  $^{13}\text{C}(\alpha, n)^{16}\text{O}$  and  $^{22}\text{Ne}(\alpha, n)^{25}\text{Mg}$ . The former reaction dominates the low-mass AGB stars, while the latter is mainly found in massive AGB stars

(Cristallo et al. 2015). As the number of free neutrons per iron seed increases, the  $s$ -process flow first seeds the light  $s$ -process peak (Sr–Y–Zr), extending to  $^{136}\text{Ba}$ , and then reaches the heavy  $s$ -process peak (Ba–La–Ce–Pr–Nd), extending to  $^{204}\text{Pb}$ – $^{207}\text{Pb}$  (Bisterzo et al. 2014).

Nucleosynthetic models indicate that Ce is mostly produced by the  $s$ -process inside AGB stars (Kobayashi et al. 2020). Bisterzo et al. (2014) estimated that 83% of the Ce in our Sun is produced by the  $s$ -process, which is comparable to other typical  $s$ -process-dominated elements; for example, Ba (85%). The

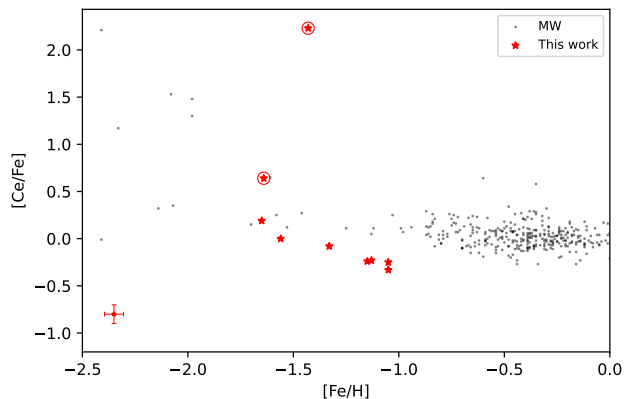


Fig. 6. [Ce/Fe] vs. [Fe/H]. Symbols are the same as in Fig. 3.

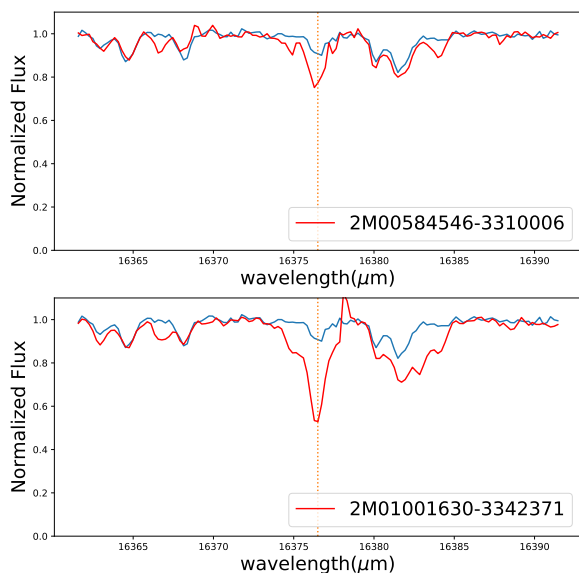


Fig. 7. Spectra of two Ce-strong stars (red lines). ( $T_{\text{eff}}$ ,  $\log g$ ,  $[\text{Fe}/\text{H}]$ ) = (4023.17 K, 0.5, -1.64) and (3959.43 K, 0.38, -1.43) for 2M00584546-3310006 and 2M01001630-3342371, respectively. A star (2M01001215-3337260) with similar stellar parameters (4107.19 K, 0.50, -1.65) is also plotted (blue lines) for comparison. The orange dotted lines mark the center of the Ce feature.

Ce abundances of our Scl stars are compared with MW stars in Fig. 6. Two stars are found to have exceptionally large  $[\text{Ce}/\text{Fe}]$ , where strong Ce lines in the spectra (Fig. 7) support the abundance credibility. More interestingly, these stars also have large  $[\text{C}/\text{Fe}]$  and  $[\text{N}/\text{Fe}]$  abundances; we further discuss these in Sect. 4.3. After excluding the two stars with the strongest  $[\text{Ce}/\text{Fe}]$ , a decreasing trend as a function of metallicity seems to exist. However, this trend is rather uncertain because of the low number statistics and the weakness of Ce lines. On the other hand, another typical  $s$ -process element, Ba, shows an increasing trend as  $[\text{Fe}/\text{H}]$  increases for Scl stars (H19); Ce in other dwarf galaxies with larger galaxy mass than Scl also shows an increasing trend as a function of metallicity (Hasselquist et al. 2021). Further high-S/N spectra with measurable Ce lines are needed to confirm this trend.

## 4. Discussion

### 4.1. Chemical evolution model

Scl has been studied extensively using different galaxy chemical evolution (GCE) models. Here, we test whether our new NIR measurements of different element abundances are consistent with the expected element abundance ratios given by GCE calculations. In particular, we calculate the evolution of  $[\text{Al}/\text{Fe}]$  and  $[\text{O}/\text{Fe}]$  values of Scl and compare them with observations for the first time. We used the publicly available GCE code ‘‘GalIMF’’ (Yan et al. 2017, 2019) to generate possible evolution tracks of element abundance ratios. The code adopts an empirically calibrated environment-dependent IMF variation law (the IGIMF theory, Kroupa et al. 2013; Jeřábková et al. 2018; Yan et al. 2020), which becomes top light in galaxies with a low star formation rate (SFR; Lee et al. 2009; Yan et al. 2020; Mucciarelli et al. 2021). The SN Ia rate in the GalIMF code is a function of the IMF because the number of potential SN Ia progenitor stars depends on it (Yan et al. 2019, 2021). We adopt the yield tables in Karakas (2010), Limongi & Chieffi (2018), and Iwamoto et al. (1999) for AGB, SN II, and SN Ia, respectively. More details of our GCE model are provided in Appendix A.

We assume a delayed- $\tau$  star formation history (Eq. A.1) that is similar to previous GCE studies of Scl (Vincenzo et al. 2014; de los Reyes et al. 2022, see Fig. A.1). The resulting time-integrated galaxy-wide IMF has a top-light shape similar to the power-law IMF with a power index for massive stars of about  $-2.7$  (see Section A.2.2). Different SN Ia delay times ( $t_{\text{delay,min}} = 40, 100, \text{ and } 400$  Myr in Eq. A.2) are tested and  $t_{\text{delay,min}} = 100$  Myr is preferred, in agreement with de los Reyes et al. (2022). The present-day stellar mass,  $2.61 \cdot 10^6 M_{\odot}$ , and the mean stellar metallicity,  $[\text{Fe}/\text{H}] = -1.67$ , of our best-fit model fit well with the literature values (see Section A.2.1 and Kirby et al. 2011).

The best-fit evolution tracks of element abundance ratios ( $[\text{O}/\text{Fe}]$ ,  $[\text{Mg}/\text{Fe}]$ ,  $[\text{Si}/\text{Fe}]$ ,  $[\text{Ca}/\text{Fe}]$ , and  $[\text{Al}/\text{Fe}]$ ) are demonstrated (Fig. 8) together with our measurement values listed in Table 2. Results of previous GCE studies of Scl are shown for comparison (the dotted-line model in Vincenzo et al. 2014, their figure 3 and the fiducial model in de los Reyes et al. 2022). The ‘‘knee’’ of the evolution tracks at about  $[\text{Fe}/\text{H}] \approx -1.5$  is caused by an increased ratio between SN Ia and SN II after the peak SFR, but this feature is not prominent (cf. Vincenzo et al. 2014 and de los Reyes et al. 2022). The evolution of  $[\text{Ti}/\text{Fe}]$ ,  $[\text{Cr}/\text{Fe}]$ ,  $[\text{Mn}/\text{Fe}]$ ,  $[\text{Ni}/\text{Fe}]$ , and  $[\text{Ce}/\text{Fe}]$  is not shown because these have a larger observational uncertainty or stellar yield uncertainty.

The measured evolution of  $[\text{O}/\text{Fe}]$ ,  $[\text{Si}/\text{Fe}]$ , and  $[\text{Ca}/\text{Fe}]$  shows good agreement with our GCE model (Fig. 8). Similar to previous studies (Lanfranchi & Matteucci 2004; Fenner et al. 2006; Romano & Starkenburg 2013; Côté et al. 2017), the  $[\text{Mg}/\text{Fe}]$  value from our best-fit model appears to be about 0.3 dex lower than the observed values, which cannot be improved without applying certain modifications of the adopted yield table (c.f. de los Reyes et al. 2022). The Al yield appears to face a similar problem, although not as significant as that found for the Mg yield. The systematic difference between the measured and calculated evolution of  $[\text{Mg}/\text{Fe}]$  and  $[\text{Al}/\text{Fe}]$  suggests problems in either the adopted stellar element yield tables or the measurements, which requires further investigation in the future.

**Table 4.** Results of linear least squares regression for each panel in Fig. 9

element	k (dex/degree)	k error (dex/degree)	r-value	p-value
[Fe/H]	-0.536	0.21859	-0.358	0.019
[O/Fe]	0.175	0.13338	0.201	0.197
[Mg/Fe]	0.399	0.13371	0.461	0.005
[Al/Fe]	0.261	0.17559	0.244	0.145
[Si/Fe]	0.138	0.07194	0.286	0.063
[Ca/Fe]	0.622	0.2038	0.506	0.005

Notes: k: best-fit slope . k error: error of the best-fit slope. r-value: linear correlation coefficient.  
p-value: two-sided p-value for a hypothesis test in which the null hypothesis is that the slope is zero.

#### 4.2. Radial chemical gradients

Bettinelli et al. (2019) suggested that the star formation history of Scl may change radially: the innermost region is expected to have undergone a longer period of star formation ( $\sim 1.5$  Gyr) compared to the outermost region ( $\sim 0.5$  Gyr). Given that star formation strongly influences chemical abundances, chemical gradients are helpful to disentangle the detailed evolution of galaxies. For example, using open clusters and young field stars in the Galactic disc, Magrini et al. (2017) confirmed the negative radial gradient of [Fe/H], and discovered positive radial gradients for [O/Fe], [Si/Fe], and [Ca/Fe], and a flat radial gradient for [Mg/Fe].

In this work, we discuss the radial chemical gradients of Scl for the first time thanks to the wide spatial coverage of our sample stars. We plot [Fe/H], [O/Fe], [Mg/Fe], [Al/Fe], [Si/Fe], and [Ca/Fe] as a function of elliptical radius in Fig. 9. Other elements are not discussed here because of insufficient data. To explore the correlations between abundances and elliptical radius, we performed linear least squares regression for each panel, and we list their slopes (k), slope errors, r-values (correlation coefficients), and p-value<sup>3</sup> in Table 4. Tolstoy et al. (2004) found a negative radial metallicity gradient in Scl using the Ca II triplet. Interestingly, there is a visible slope change around  $0.2^\circ$  in elliptical radius (their Fig. 3). Our results agree with those of Tolstoy et al. (2004): the p-value = 0.019 and  $k = -0.536$  that we find suggest a negative radial metallicity gradient, and there is a hint that the slope becomes flatter beyond  $0.2^\circ$  elliptical radius. On the other hand, our linear regression analysis (Table 4) suggests a nondetectable radial gradient of [O/Fe], [Al/Fe], and [Si/Fe], as their two-sided p-value is too large. Meanwhile, [Mg/Fe] and [Ca/Fe] show positive radial gradients (positive slope values), albeit with large scatter ( $0.4 < r\text{-value} \lesssim 0.5$ ). The two-sided p-values are less than 0.05, indicating reliable correlations. The radial metallicity gradient and radial gradients of [Mg/Fe] and [Ca/Fe] can be explained by the outside-in scenario proposed by Bettinelli et al. (2019) and also found in other dwarf galaxies in the Local Group (Hidalgo et al. 2013). The prolonged star formation in the innermost region ( $\sim 1.5$  Gyr, Bettinelli et al. 2019) generates comparatively more iron, causing higher [Fe/H], and comparatively lower [Mg/Fe] and [Ca/Fe]. A chemical evolution model with radial distribution will be the helpful to quantify these.

<sup>3</sup> A hypothesis test, whereby the null hypothesis is that the slope is zero, using Wald Test with t-distribution of the test statistic.

#### 4.3. Stars with enhanced Ce

As we discuss in Section 3, two stars show enhanced C, N, and Ce, which is a strong hint of AGB stars. Their chemical abundances are compared to those suggested by the AGB model of  $1.3 M_\odot$ ,  $Z=0.0001^4$  (Cristallo et al. 2011). To minimize the impact of chemical abundances inherited from the original cloud, the median of a given element ( $[X/Fe]_{median}$ ) is subtracted from the measured abundance<sup>5</sup> (Fig. 10). AGB stars going through third dredge-up (TDU) experience multiple episodes, where chemical composition changes accordingly. A good match between observations and models is seen in 2M00584546-3310006, while 2M01001630-3342371 detects higher N and Ce abundances than suggested by AGB models. More massive models or models with different metallicities do not seem to fully reconcile the discrepancies. AGB models of  $< 1.3 M_\odot$  or binary models may be needed to explain such high N and Ce abundances.

#### 4.4. N-rich field stars

The recently found N-rich field stars in the MW (Martell & Grebel 2010; Fernández-Trincado et al. 2017; Tang et al. 2019; Fernández-Trincado et al. 2019a; Tang et al. 2020) have fuelled debate as to their origin. It is suggested that most N-rich field stars may be formed in the dense environment of globular clusters (Martell & Grebel 2010; Tang et al. 2020), while some of them are generated in binary systems (Fernández-Trincado et al. 2019b). According to chemo-dynamical analysis of N-rich field stars, a substantial portion of them may have an extragalactic origin (Tang et al. 2020; Yu et al. 2021; Fernández-Trincado et al. 2022). Fernández-Trincado et al. (2021, 2020) reported the discovery of a large group of N-rich field stars in Sgr and Magellanic Clouds.

In this work, we find most of the  $^{12}\text{C}^{14}\text{N}$  molecular lines are too weak to give meaningful results, except for three stars with exceptionally large [N/Fe]. As mentioned in Section 4.3, two stars with strong C, N, and Ce are likely AGB stars. While the third star, 2M00591209-3346208, does show large [N/Fe] ( $\sim 1.4$ ), its [C/Fe] is also quite large ( $\sim 0.6$ ). This star therefore fails to satisfy one of the criteria of N-rich field stars ( $[C/Fe] < 0.15$ , Schiavon et al. 2017; Fernández-Trincado et al. 2019a). Given that the nondetection of strong  $^{12}\text{C}^{14}\text{N}$  molecular lines in other Scl stars excludes the possibility of them being N-rich field stars,

<sup>4</sup> <http://fruity.oa-teramo.inaf.it/modelli.pl>

<sup>5</sup> Because N abundances are only measured in three stars, and they do not reflect the original abundances of the cloud; we therefore use  $[X/Fe]_{median} = 0.5$  instead.

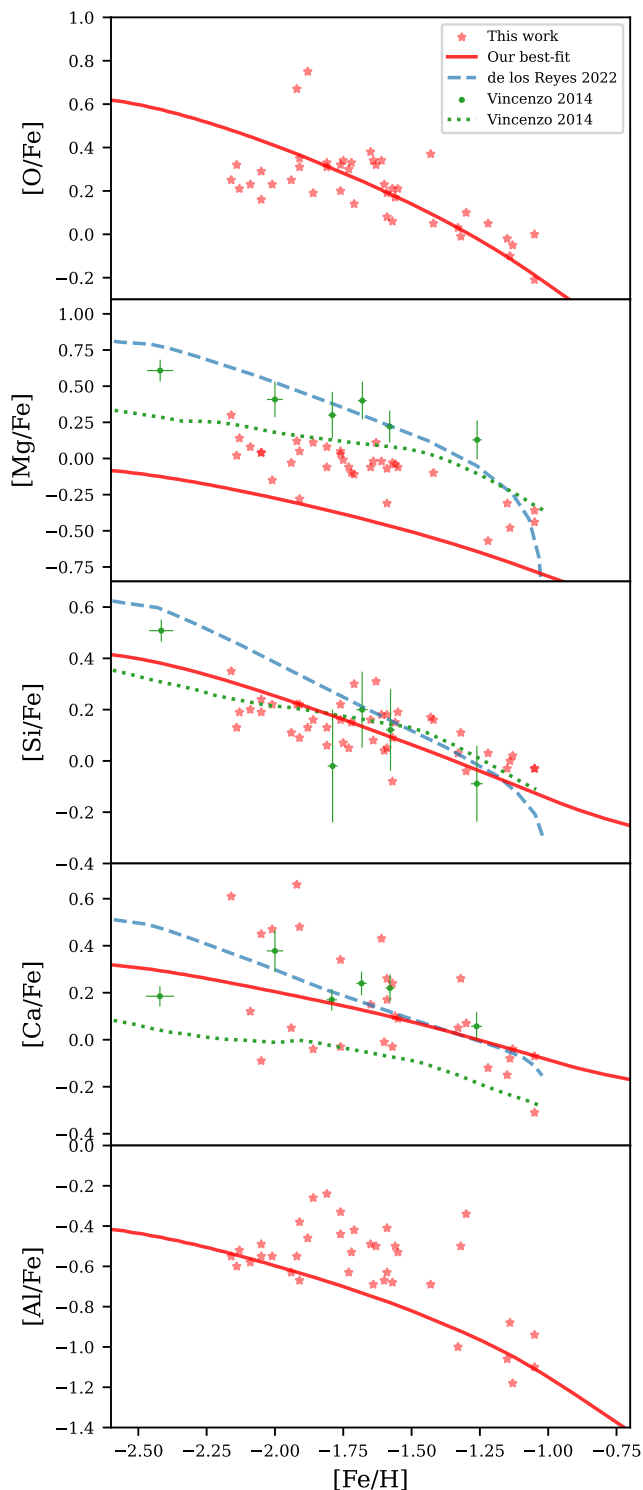


**Fig. 8.** Evolution of  $[X/Fe]$ - $[Fe/H]$  relations of our best-fit GCE model (red curves) in comparison with observations (red stars, Table 2). The green dots are data compiled in Vincenzo et al. (2014). The green dotted curves and blue dashed curves are the dotted-line model in Vincenzo et al. (2014, their figure 3,) and the fiducial model in de los Reyes et al. (2022), respectively.

we conclude that no N-rich field stars are detected in our Scl sample. Our result is consistent with that of Lardo et al. (2016), who used optical CN and CH bands around 4000 Å to investi-

gate the C and N abundances of Scl stars. The lack of N-rich field stars in Scl may indicate that this dwarf galaxy is deficient of very dense star forming environments (e.g., globular clusters).

## 5. Conclusions

Dissolved and existing dwarf galaxies are the basic building blocks of our past, present, and future MW. The detailed evolutionary history of galaxy formation is imprinted in chemical abundances, waiting to be decoded. In this work, we analyze C, N, O, Mg, Al, Si, Ca, Ti, Cr, Fe, Mn, Ni, and Ce of 43 giant stars in Scl using NIR APOGEE spectra. Precise O, Si, and Al abundances are determined in an unprecedented sample size of stars (~40), thanks to the strong feature lines in APOGEE spectra. After comparing with abundances obtained from optical spectra, there is generally good agreement, except for  $[Mg/Fe]$ .  $[\alpha/Fe]$  of Scl stars is systematically lower than in MW field stars or Sgr stars, confirming the observed trend that less massive galaxies show lower  $[\alpha/Fe]$ .  $[Al/Fe]$  shows a decreasing trend as a function of metallicity, with a median value of about -0.5, providing an excellent indicator with which to distinguish Scl stars from the field stars of the MW.

The observed abundance ratios are compared with the calculated chemical evolution of Scl assuming an environment-dependent IMF given by IGIMF theory. Similar to previous GCE studies, our model favors a top-light IMF with a high-mass IMF power index of about -2.7 and a minimum SN Ia delay time of about 100 Myr. The expected evolution tracks of  $[O/Fe]$ ,  $[Si/Fe]$ , and  $[Ca/Fe]$  from the GCE model agree well with our observation. With the Al abundances of a large number of stars in Scl measured for the first time, we find that the GCE-predicted  $[Al/Fe]$  evolution track is consistent with observations. However, the observed  $[Al/Fe]$  values are generally higher than those predicted by the GCE.

Our linear regression analysis suggests a negative radial metallicity gradient in Scl, spanning up to 0.9 degrees in elliptical radius.  $[Mg/Fe]$  and  $[Ca/Fe]$  show increasing trends as a function of metallicity. These are consistent with the inside-out formation scenario, which suggests the quenching of star formation toward the center as the galaxy runs out of gas in the outskirts. Furthermore, we detect no N-rich field stars in our sample, indicating that Scl may be deficient in very dense star forming environment. In the near future, the China Space Station Telescope (CSST), equipped with the most advanced ultraviolet and optical photometric and spectroscopic system, will have a significant impact on the investigation of the star formation history across dwarf galaxies, the search for N-rich field stars and AGB stars, and so on.

## Acknowledgments

We thank Thomas Masseron, Gary Da Costa, Yang Huang for helpful discussions. We thank the anonymous referee for insightful comments. B.T. and J.Z. gratefully acknowledge support from the National Natural Science Foundation of China under grant No. U1931102, the China Manned Space Project NO. CMS-CSST-2021-B03, the Natural Science Foundation of Guangdong Province under grant No. 2022A1515010732, the National Natural Science Foundation of China through grants No. 12233013, and the Fundamental Research Funds for the Central Universities, Sun Yat-sen University under No. 22qntd3101. Z.Y. acknowledges support from the Fundamental Research Funds for the Central Universities under grant

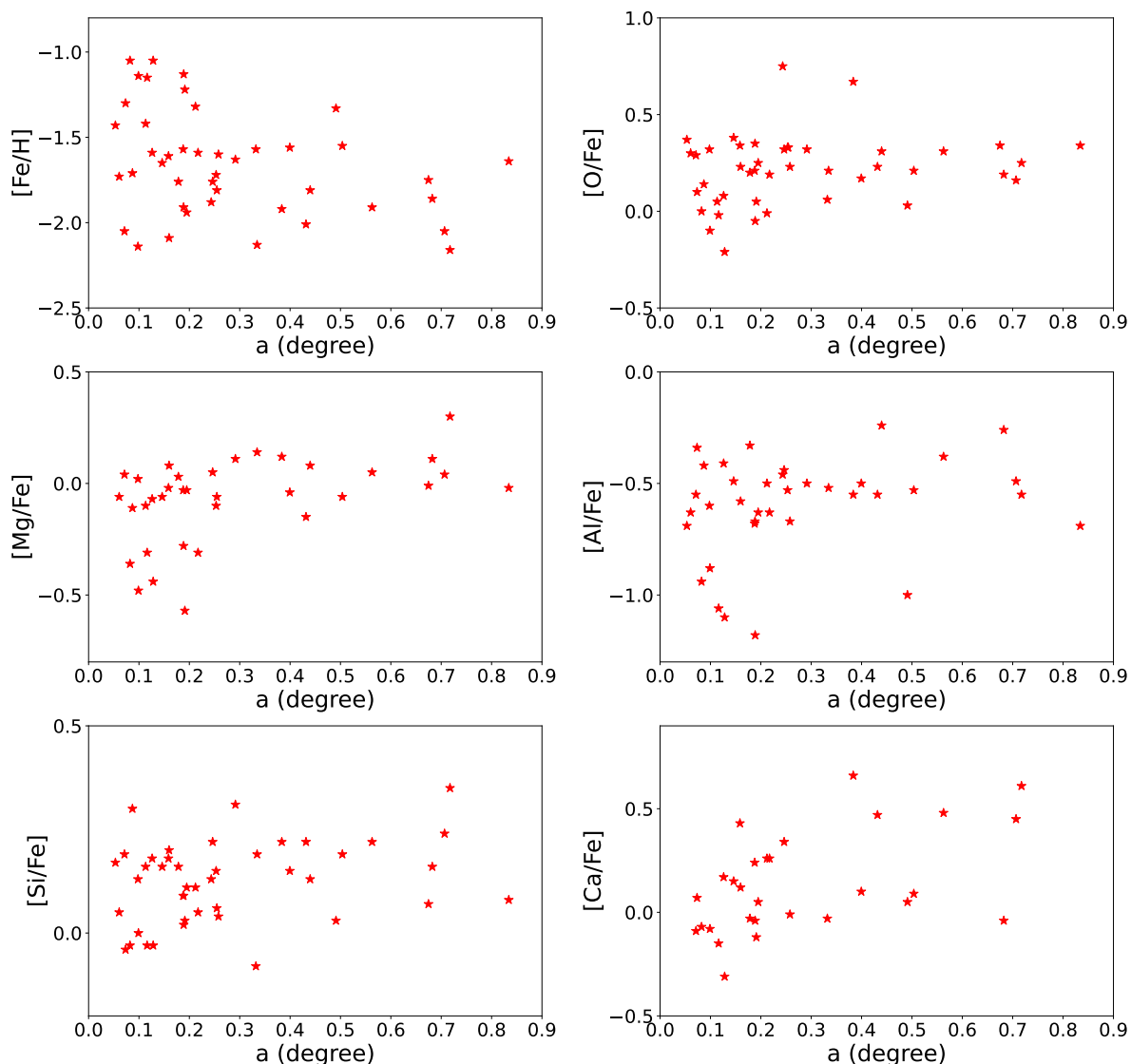


**Fig. 9.** Element abundances as a function of elliptical radius in degrees.

number 0201/14380049, support through the Jiangsu Funding Program for Excellent Postdoctoral Talent under grant number 2022ZB54, and support of the National Natural Science Foundation of China under grant No. 12203021. Z.Z. and Z.Y. acknowledge the support of the National Natural Science Foundation of China under grants No. 12041305, 12173016, the Program for Innovative Talents, Entrepreneurs in Jiangsu, the science research grants from the China Manned Space Project with NO.CMS-CSST-2021-A08 (IMF), and the science research grants from the China Manned Space Project with NO.CMS-CSST-2021-A07 (lensing). The development of our chemical evolution model applied in this work (GalIMF) benefited from the International Space Science Institute (ISSI/ISSI-BJ) in Bern

and Beijing, thanks to the funding of the team “Chemical abundances in the ISM: the litmus test of stellar IMF variations in galaxies across cosmic time” (Donatella Romano and Zhi-Yu Zhang). J.G.F-T gratefully acknowledges the grant support provided by Proyecto Fondecyt Iniciación No. 11220340, and also from ANID Concurso de Fomento a la Vinculación Internacional para Instituciones de Investigación Regionales (Modalidad corta duración) Proyecto No. FOVI210020, and from the Joint Committee ESO-Government of Chile 2021 (ORP 023/2021), and from Becas Santander Movilidad Internacional Profesores 2022, Banco Santander Chile.

Funding for the Sloan Digital Sky Survey IV has been provided by the Alfred P. Sloan Foundation, the U.S. Department

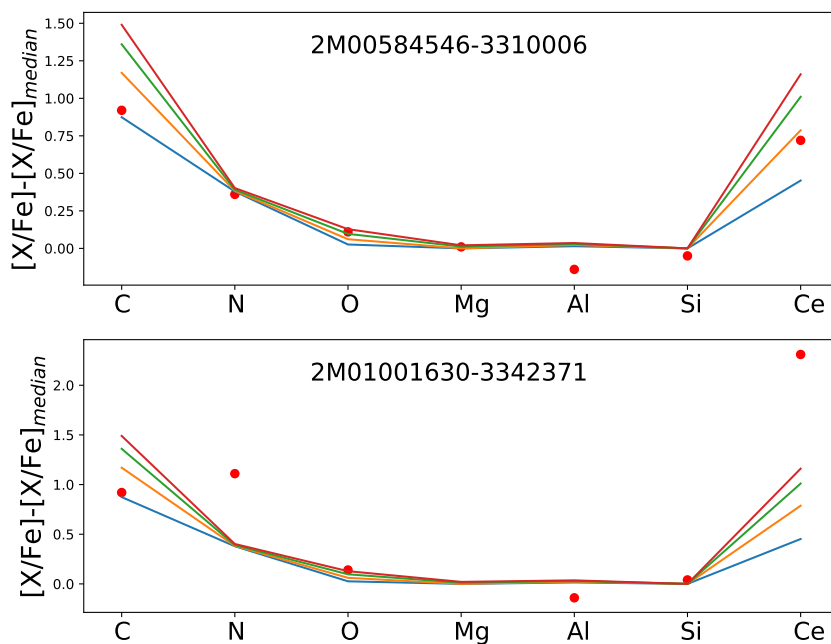


**Fig. 10.** Chemical abundances of two Ce-enhanced stars (red dots) compared with the AGB model of  $1.3 M_{\odot}$ ,  $Z=0.0001$ . Models of second, third, fourth, and fifth episodes of third dredge-up are shown as blue, orange, green, and red lines, respectively.

of Energy Office of Science, and the Participating Institutions. SDSS-IV acknowledges support and resources from the Center for High-Performance Computing at the University of Utah. The SDSS website is <http://www.sdss.org>.

SDSS-IV is managed by the Astrophysical Research Consortium for the Participating Institutions of the SDSS Collaboration including the Brazilian Participation Group, the Carnegie Institution for Science, Carnegie Mellon University, the Chilean Participation Group, the French Participation Group, Harvard-Smithsonian Center for Astrophysics, Instituto de Astrofísica de Canarias, The Johns Hopkins University, Kavli Institute for the Physics and Mathematics of the Universe (IPMU) / University of Tokyo, Lawrence Berkeley National Laboratory, Leibniz Institut für Astrophysik Potsdam (AIP), Max-Planck-Institut für Astronomie (MPIA Heidelberg), Max-Planck-Institut für Astrophysik (MPA Garching), Max-Planck-Institut für Extraterrestrische Physik (MPE), National Astronomical Observatory of China, New Mexico State University, New York University, University of Notre Dame, Observatório Nacional / MCTI, The Ohio State University, Pennsylvania State University, Shanghai Astronomical Observatory, United Kingdom Participation Group, Universidad Nacional Autónoma de México, University of Arizona, University of Colorado Boulder, University of Oxford, University of Portsmouth, University of Utah, University of Virginia, University of Washington, University of Wisconsin, Vanderbilt University, and Yale University.

## References

- Abdurro'uf, Accetta, K., Aerts, C., et al. 2022, *ApJS*, 259, 35  
 Allende Prieto, C., Beers, T. C., Wilhelm, R., et al. 2006, *ApJ*, 636, 804  
 Alonso, A., Arribas, S., & Martínez-Roger, C. 1999, *A&AS*, 140, 261  
 Alvarez, R. & Plez, B. 1998, *A&A*, 330, 1109  
 Andrievsky, S. M., Spite, M., Korotin, S. A., et al. 2008, *A&A*, 481, 481  
 Arnett, W. D. 1971, *ApJ*, 166, 153  
 Arnould, M., Goriely, S., & Jorissen, A. 1999, *A&A*, 347, 572  
 Asplund, M., Grevesse, N., & Sauval, A. J. 2005, in *Astronomical Society of the Pacific Conference Series*, Vol. 336, *Cosmic Abundances as Records of Stellar Evolution and Nucleosynthesis*, ed. I. Barnes, Thomas G. & F. N. Bash, 25  
 Barklem, P. S., Christlieb, N., Beers, T. C., et al. 2005, *A&A*, 439, 129  
 Beaton, R. L., Oelkers, R. J., Hayes, C. R., et al. 2021, *AJ*, 162, 302  
 Belokurov, V., Erkal, D., Evans, N. W., Koposov, S. E., & Deason, A. J. 2018, *MNRAS*, 478, 611  
 Bensby, T., Feltzing, S., & Oey, M. S. 2014, *A&A*, 562, A71  
 Bettinelli, M., Hidalgo, S. L., Cassisi, S., et al. 2019, *MNRAS*, 487, 5862  
 Bisterzo, S., Travaglio, C., Gallino, R., Wiescher, M., & Käppeler, F. 2014, *ApJ*, 787, 10  
 Blanton, M. R., Bershady, M. A., Abolfathi, B., et al. 2017, *AJ*, 154, 28  
 Bowen, I. S. & Vaughan, A. H., J. 1973, *Appl. Opt.*, 12, 1430  
 Busso, M., Gallino, R., Lambert, D. L., Travaglio, C., & Smith, V. V. 2001, *ApJ*, 557, 802  
 Cayrel, R., Depagne, E., Spite, M., et al. 2004, *A&A*, 416, 1117  
 Colavitti, E., Pipino, A., & Matteucci, F. 2009, *A&A*, 499, 409  
 Coleman, M. G., Da Costa, G. S., & Bland-Hawthorn, J. 2005, *AJ*, 130, 1065  
 Côté, B., Fryer, C. L., Belczynski, K., et al. 2018, *ApJ*, 855, 99  
 Côté, B., O'Shea, B. W., Ritter, C., Herwig, F., & Venn, K. A. 2017, *ApJ*, 835, 128  
 Cristallo, S., Piersanti, L., Straniero, O., et al. 2011, *ApJS*, 197, 17  
 Cristallo, S., Straniero, O., Piersanti, L., & Gobrecht, D. 2015, *ApJS*, 219, 40  
 Das, P., Hawkins, K., & Jofré, P. 2020, *MNRAS*, 493, 5195  
 de los Reyes, M. A. C., Kirby, E. N., Ji, A. P., & Nuñez, E. H. 2022, *ApJ*, 925, 66  
 de los Reyes, M. A. C., Kirby, E. N., Seitzzahl, I. R., & Shen, K. J. 2020, *ApJ*, 891, 85  
 Duggan, G. E., Kirby, E. N., Andrievsky, S. M., & Korotin, S. A. 2018, *ApJ*, 869, 50  
 Eisenstein, D. J., Weinberg, D. H., Agol, E., et al. 2011, *AJ*, 142, 72  
 Faber, S. M., Phillips, A. C., Kibrick, R. I., et al. 2003, in *Society of Photo-Optical Instrumentation Engineers (SPIE) Conference Series*, Vol. 4841, *Instrument Design and Performance for Optical/Infrared Ground-based Telescopes*, ed. M. Iye & A. F. M. Moorwood, 1657–1669  
 Fenner, Y., Gibson, B. K., Gallino, R., & Lugaro, M. 2006, *ApJ*, 646, 184  
 Fernández-Trincado, J. G., Beers, T. C., Barbuy, B., et al. 2022, *A&A*, 663, A126  
 Fernández-Trincado, J. G., Beers, T. C., Minniti, D., et al. 2020, *ApJ*, 903, L17



- Fernández-Trincado, J. G., Beers, T. C., Minniti, D., et al. 2021, *A&A*, 648, A70
- Fernández-Trincado, J. G., Beers, T. C., Tang, B., et al. 2019a, *MNRAS*, 488, 2864
- Fernández-Trincado, J. G., Mennickent, R., Cabezas, M., et al. 2019b, *A&A*, 631, A97
- Fernández-Trincado, J. G., Zamora, O., García-Hernández, D. A., et al. 2017, *ApJ*, 846, L2
- Freundlich, J. & Maoz, D. 2021, *MNRAS*, 502, 5882
- Friedmann, M. & Maoz, D. 2018, *MNRAS*, 479, 3563
- Fulbright, J. P. 2000, *AJ*, 120, 1841
- Gaia Collaboration, Helmi, A., van Leeuwen, F., et al. 2018, *A&A*, 616, A12
- Geha, M., Brown, T. M., Tumlinson, J., et al. 2013, *ApJ*, 771, 29
- Geisler, D., Smith, V. V., Wallerstein, G., Gonzalez, G., & Charbonnel, C. 2005, *AJ*, 129, 1428
- Grebel, E. K., Gallagher, John S., I., & Harbeck, D. 2003, *AJ*, 125, 1926
- Gunn, J. E., Siegmund, W. A., Mannery, E. J., et al. 2006, *AJ*, 131, 2332
- Gustafsson, B., Edvardsson, B., Eriksson, K., et al. 2008, *A&A*, 486, 951
- Hasselquist, S., Hayes, C. R., Lian, J., et al. 2021, *ApJ*, 923, 172
- Hasselquist, S., Shetrone, M., Smith, V., et al. 2017, *ApJ*, 845, 162
- Helmi, A., Babusiaux, C., Koppelman, H. H., et al. 2018, *Nature*, 563, 85
- Hidalgo, S. L., Monelli, M., Aparicio, A., et al. 2013, *ApJ*, 778, 103
- Hill, V., Skúladóttir, Á., Tolstoy, E., et al. 2019, *A&A*, 626, A15
- Isobe, Y., Ouchi, M., Nakajima, K., et al. 2022, arXiv e-prints, arXiv:2206.04709
- Iwamoto, K., Brachwitz, F., Nomoto, K., et al. 1999, *ApJS*, 125, 439
- Jablunka, P., North, P., Mashonkina, L., et al. 2015, *A&A*, 583, A67
- Jefábková, T., Hasani Zonoozi, A., Kroupa, P., et al. 2018, *A&A*, 620, A39
- Kajino, T., Aoki, W., Balantekin, A. B., et al. 2019, *Progress in Particle and Nuclear Physics*, 107, 109
- Karakas, A. I. 2010, *MNRAS*, 403, 1413
- Karakas, A. I. & Lattanzio, J. C. 2014, *PASA*, 31, e030
- Kirby, E. N., Guhathakurta, P., Simon, J. D., et al. 2010, *ApJS*, 191, 352
- Kirby, E. N., Guo, M., Zhang, A. J., et al. 2015, *ApJ*, 801, 125
- Kirby, E. N., Lanfranchi, G. A., Simon, J. D., Cohen, J. G., & Guhathakurta, P. 2011, *ApJ*, 727, 78
- Kirby, E. N., Xie, J. L., Guo, R., Kovalev, M., & Bergemann, M. 2018, *ApJS*, 237, 18
- Kobayashi, C., Karakas, A. I., & Lugaro, M. 2020, *ApJ*, 900, 179
- Kroupa, P. 2001, *MNRAS*, 322, 231
- Kroupa, P. 2002, *Science*, 295, 82
- Kroupa, P., Tout, C. A., & Gilmore, G. 1993, *MNRAS*, 262, 545
- Kroupa, P., Weidner, C., Pflamm-Altenburg, J., et al. 2013, in *Planets, Stars and Stellar Systems. Volume 5: Galactic Structure and Stellar Populations*, ed. T. D. Oswalt & G. Gilmore, Vol. 5, 115
- Lanfranchi, G. A. & Matteucci, F. 2004, *MNRAS*, 351, 1338
- Lardo, C., Battaglia, G., Pancino, E., et al. 2016, *A&A*, 585, A70
- Law, D. R. & Majewski, S. R. 2010, *ApJ*, 718, 1128
- Lee, J. C., Gil de Paz, A., Tremonti, C., et al. 2009, *ApJ*, 706, 599
- Limongi, M. & Chieffi, A. 2018, *ApJS*, 237, 13
- Lind, K., Nordlander, T., Wehrhahn, A., et al. 2022, arXiv e-prints, arXiv:2206.11070
- Magrini, L., Randich, S., Kordopatis, G., et al. 2017, *A&A*, 603, A2
- Majewski, S. R., Schiavon, R. P., Frinchaboy, P. M., et al. 2017, *AJ*, 154, 94
- Majewski, S. R., Skrutskie, M. F., Weinberg, M. D., & Ostheimer, J. C. 2003, *ApJ*, 599, 1082
- Maoz, D. & Mannucci, F. 2012, *PASA*, 29, 447
- Martell, S. L. & Grebel, E. K. 2010, *A&A*, 519, A14
- Mashonkina, L., Jablunka, P., Sitnova, T., Pakhomov, Y., & North, P. 2017, *A&A*, 608, A89
- Masseron, T., Merle, T., & Hawkins, K. 2016, *BACCHUS: Brussels Automatic Code for Characterizing High accUracy Spectra*
- Masseron, T., Osorio, Y., García-Hernández, D. A., et al. 2021, *A&A*, 647, A24
- Mateo, M. L. 1998, *ARA&A*, 36, 435
- Matteucci, F. & Greggio, L. 1986, *A&A*, 154, 279
- Minelli, A., Mucciarelli, A., Romano, D., et al. 2021, *ApJ*, 910, 114
- Muñoz, R. R., Côté, P., Santana, F. A., et al. 2018a, *ApJ*, 860, 65
- Muñoz, R. R., Côté, P., Santana, F. A., et al. 2018b, *ApJ*, 860, 66
- Mucciarelli, A., Massari, D., Minelli, A., et al. 2021, *Nature Astronomy*, 5, 1247
- Myeong, G. C., Vasiliev, E., Iorio, G., Evans, N. W., & Belokurov, V. 2019, *MNRAS*, 488, 1235
- Nidever, D. L., Holtzman, J. A., Allende Prieto, C., et al. 2015, *AJ*, 150, 173
- Nissen, P. E. & Schuster, W. J. 2011, *A&A*, 530, A15
- Nomoto, K., Iwamoto, K., Nakasato, N., et al. 1997, *Nuclear Physics A*, 621, 467
- Nomoto, K., Kobayashi, C., & Tominaga, N. 2013, *ARA&A*, 51, 457
- Osorio, Y., Allende Prieto, C., Hubeny, I., Mészáros, S., & Shetrone, M. 2020, *A&A*, 637, A80
- Pietrzyński, G., Gieren, W., Szewczyk, O., et al. 2008, *AJ*, 135, 1993
- Plez, B. 2012, *Turbospectrum: Code for spectral synthesis*, *Astrophysics Source Code Library*
- Ramírez, I. & Meléndez, J. 2005, *ApJ*, 626, 465
- Reddy, B. E., Lambert, D. L., & Allende Prieto, C. 2006, *MNRAS*, 367, 1329
- Reddy, B. E., Tomkin, J., Lambert, D. L., & Allende Prieto, C. 2003, *MNRAS*, 340, 304
- Reichert, M., Hansen, C. J., Hanke, M., et al. 2020, *A&A*, 641, A127
- Ritter, C., Côté, B., Herwig, F., Navarro, J. F., & Fryer, C. L. 2018, *ApJS*, 237, 42
- Roederer, I. U., Preston, G. W., Thompson, I. B., et al. 2014, *AJ*, 147, 136
- Romano, D. & Starkenburg, E. 2013, *MNRAS*, 434, 471
- Santana, F. A., Beaton, R. L., Covey, K. R., et al. 2021, *AJ*, 162, 303
- Schiavon, R. P., Zamora, O., Carrera, R., et al. 2017, *MNRAS*, 465, 501
- Schlegel, D. J., Finkbeiner, D. P., & Davis, M. 1998, *ApJ*, 500, 525
- Shetrone, M., Venn, K. A., Tolstoy, E., et al. 2003, *AJ*, 125, 684
- Simon, J. D., Jacobson, H. R., Frebel, A., et al. 2015, *ApJ*, 802, 93
- Smith, V. V., Cunha, K., Shetrone, M. D., et al. 2013, *ApJ*, 765, 16
- Starkenburg, E., Hill, V., Tolstoy, E., et al. 2013, *A&A*, 549, A88
- Tang, B., Fernández-Trincado, J. G., Liu, C., et al. 2020, *ApJ*, 891, 28
- Tang, B., Liu, C., Fernández-Trincado, J. G., et al. 2019, *ApJ*, 871, 58
- Thielemann, F.-K., Arcones, A., Käppeli, R., et al. 2011, *Progress in Particle and Nuclear Physics*, 66, 346
- Tolstoy, E., Hill, V., Irwin, M., et al. 2006, *The Messenger*, 123, 33
- Tolstoy, E., Hill, V., & Tosi, M. 2009, *ARA&A*, 47, 371
- Tolstoy, E., Irwin, M. J., Helmi, A., et al. 2004, *ApJ*, 617, L119
- Vincenzo, F., Matteucci, F., Vattakunnel, S., & Lanfranchi, G. A. 2014, *MNRAS*, 441, 2815
- Watson, D., Hansen, C. J., Selsing, J., et al. 2019, *Nature*, 574, 497
- Weisz, D. R., Dolphin, A. E., Skillman, E. D., et al. 2014, *ApJ*, 789, 147
- Woo, J., Courteau, S., & Dekel, A. 2008, *MNRAS*, 390, 1453
- Woolsey, S. E. & Weaver, T. A. 1995, *ApJS*, 101, 181
- Woolsey, S. E., Wilson, J. R., Mathews, G. J., Hoffman, R. D., & Meyer, B. S. 1994, *ApJ*, 433, 229
- Yan, Z., Jerabkova, T., & Kroupa, P. 2017, *A&A*, 607, A126
- Yan, Z., Jerabkova, T., & Kroupa, P. 2020, *A&A*, 637, A68
- Yan, Z., Jerabkova, T., Kroupa, P., & Vazdekis, A. 2019, *A&A*, 629, A93
- Yan, Z., Jefábková, T., & Kroupa, P. 2021, *A&A*, 655, A19
- Yong, D., Norris, J. E., Bessell, M. S., et al. 2013, *ApJ*, 762, 26
- Yu, J., Tang, B., Fernández-Trincado, J. G., et al. 2021, *ApJ*, 913, 23
- Zamora, O., García-Hernández, D. A., Allende Prieto, C., et al. 2015, *AJ*, 149, 181
- Zasowski, G., Cohen, R. E., Chojnowski, S. D., et al. 2017, *AJ*, 154, 198
- Zhang, J., Shi, J., Pan, K., Allende Prieto, C., & Liu, C. 2017, *ApJ*, 835, 90

## Appendix A: GCE model

### Appendix A.1: Method

Metal-poor gas-rich dwarf galaxies are observed to be dispersion-dominated systems with high specific SFRs (Isobe et al. 2022), in agreement with the idea that spheroids are formed in a quick monolithic collapse (Colavitti et al. 2009). Under this framework, we implement a closed-box model, as described by Yan et al. (2020), to calculate the chemical evolution of Scl. We assume that a primordial gas of  $1.26 \cdot 10^8 M_\odot$  (similar to Vincenzo et al. 2014) is presented at the beginning of the simulation while there is no additional gas infall. Stars form according to a given star formation history. The SFR for each 10 Myr simulation time step,  $\bar{\psi}_{10 \text{ Myr}}$ , is given by the delayed- $\tau$  model,

$$\bar{\psi}_{10 \text{ Myr}}(t) = R \cdot t/\tau \cdot e^{-t/\tau}, \quad (\text{A.1})$$

where  $R$  and  $\tau$  are characteristic SFR and star formation timescale constants (best-fit parameter values given in Section A.2.1).

The AGB and core-collapse supernovae yields are adopted from Karakas (2010) and Limongi & Chieffi (2018), respectively, from the readily compiled yield table provided by the NuPyCEE code (Ritter et al. 2018). The IMF-weighted yields of explosive  $\alpha$  elements (Si and Ca) is more pronounced for stars between 8 and  $12 M_\odot$  in Limongi & Chieffi (2018), considering stellar rotation, relative to Nomoto et al. (2013). In general, this leads to a better fit with observed  $[X/\text{Fe}]$ – $[\text{Fe}/\text{H}]$  relations in dwarf galaxies (cf. Minelli et al. 2021). We find that a mixture of core-collapse supernova yields (averaging the yields for non-rotating stars and the yields for stars with an initial equatorial velocity of  $150 \text{ km s}^{-1}$  in Limongi & Chieffi 2018) lead to the best fit to the observed abundance ratio evolution.

For the SN Ia yield, we adopt Iwamoto et al. (1999, their W70 model). The delay time distribution (DTD) of SN Ia,  $f_{\text{delay}}(t)$ , is assumed to be a power law (Maoz & Mannucci 2012) with a variable minimum SN Ia delay time,  $t_{\text{delay,min}}$ ,

$$f_{\text{delay}}(t) = \begin{cases} 0, & t \leq t_{\text{delay,min}} \\ k [\text{yr}^{-1} M_\odot^{-1}] \cdot (t/1 \text{ Gyr})^{-1}, & t > t_{\text{delay,min}} \end{cases} \quad (\text{A.2})$$

In the above equations, the normalization parameter  $k$  determines the total number of SNe Ia, which depends on the number of available SN Ia progenitors, and therefore on the IMF. The number of SN Ia per stellar mass formed within time  $t$  after the formation of a simple stellar population,  $n_{\text{Ia}}$ , is scaled according to the IMF variation, following Yan et al. (2019, 2021). That is,

$$n_{\text{Ia}}(t, \xi) = \frac{n_{1.5, m_{\text{MWD}}}(\xi)}{M_{0.08, 150}(\xi)} \cdot \frac{n_{1.5, m_{\text{MWD}}}(\xi)}{n_{0.08, 150}(\xi)} \cdot \int_0^t f_{\text{delay}}(t) dt, \quad (\text{A.3})$$

where  $\xi$  is the IMF of the stellar population,  $m_{\text{MWD}}$  is the mass of the most massive star that can become a SN Ia progenitor,  $n$  is the number of stars within the mass range given by its subscript (in the unit of  $M_\odot$ ), and  $M$  is the mass of stars in a given mass range indicated by its subscript.

SN Ia delay times of  $t_{\text{delay,min}} = 40, 100,$  and  $400 \text{ Myr}$  are tested in the present study. As  $t_{\text{delay,min}}$  is the lifetime of the stars with mass  $m_{\text{MWD}}$  according to the stellar mass–lifetime relation (Yan et al. 2019, their figure 3), these two parameters are linked. Therefore,  $m_{\text{MWD}}$  is set to 8, 5, and  $3 M_\odot$  for these  $t_{\text{delay,min}}$  values respectively. Then, the parameter  $k$  with a given  $t_{\text{delay,min}}$  can be determined by the empirical SN Ia production efficiency given

by Maoz & Mannucci (2012), assuming the canonical Kroupa (2001) IMF,  $\xi_{\text{canonical}}$ ,

$$n_{\text{Ia}}(t = 10 \text{ Gyr}, \xi_{\text{canonical}}) = 0.002/M_\odot. \quad (\text{A.4})$$

See also Friedmann & Maoz (2018), Freundlich & Maoz (2021), and Yan et al. (2021) for additional observational constraints on the SN Ia production efficiency. Therefore,  $k$  is first calibrated for a given  $t_{\text{delay,min}}$  value, assuming the canonical IMF. It turns out that the  $t_{\text{delay,min}} = 100 \text{ Myr}$  model fits best with the observed shape of  $[\text{X}/\text{Fe}]$ – $[\text{Fe}/\text{H}]$  relations, which is consistent with the findings of de los Reyes et al. (2022). For  $t_{\text{delay,min}} = 100 \text{ Myr}$ ,  $k \approx 4.27 \cdot 10^{-13} [\text{yr}^{-1} M_\odot^{-1}]$  (cf. Maoz & Mannucci 2012, their equation 13). Therefore,  $n_{\text{Ia}}(t)$  can be calculated for any variable IMF. The DTD and therefore the exact values for the lower and upper mass limit for SN Ia progenitors ( $1.5$  and  $m_{\text{MWD}}$ ) are not well constrained by observations. Fortunately, the calculation result of Eq. A.3 is not sensitive to these mass limits (cf. Yan et al. 2019, 2021).

### Appendix A.2: Best-fit result

#### Appendix A.2.1: Star formation history

The star formation history of our best-fit model is shown in Fig. A.1. With the star formation history parameters (Eq. A.1) being  $R = 0.05 M_\odot/\text{yr}$  and  $\tau = 150 \text{ Myr}$ . The total stellar mass ever formed is  $M_\star = \int_0^{13 \text{ Gyr}} \bar{\psi}_{10 \text{ Myr}}(t) dt = R \cdot \tau = 7.5 \cdot 10^6 M_\odot$  and the resulting present-day stellar mass is  $2.61 \cdot 10^6 M_\odot$ , which is comparable with observational values (Woo et al. 2008; Mateo 1998; Grebel et al. 2003) and previous Scl models (Vincenzo et al. 2014 and de los Reyes et al. 2022).

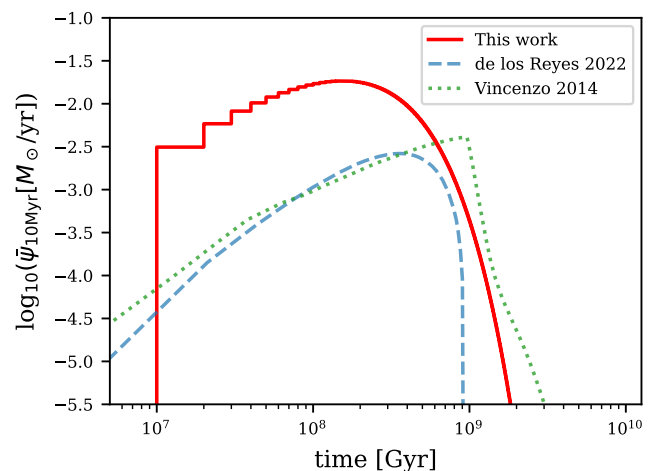


**Fig. A.1.** Star formation history of our best-fit model (red curve), formulated by the delayed- $\tau$  model (Eq. A.1). The green dotted and blue dashed curves denote the star formation history applied in Vincenzo et al. (2014) and de los Reyes et al. (2022, their fiducial model), respectively.

#### Appendix A.2.2: IMF variation

The canonical multiple-part power-law stellar IMF has the form:

$$\xi(m) = \begin{cases} k_1 m^{-\alpha_1}, & 0.08 \leq m < 0.5, \\ k_2 m^{-\alpha_2}, & 0.5 \leq m < 1, \\ k_3 m^{-\alpha_3}, & 1 \leq m < 150, \end{cases} \quad (\text{A.5})$$



where  $\alpha_1 = 1.3$  and  $\alpha_2 = \alpha_3 = 2.3$  (Kroupa 2001, 2002; Kroupa et al. 2013). The normalization parameters,  $k_1$ ,  $k_2$ , and  $k_3$  are adjusted to ensure a continuous IMF.

Figure A.2 shows the galaxy-wide IMFs at each time step and the time-integrated galaxy-wide IMF for the entire star formation history of our Scl model, calculated with the IGIMF formulation given in Yan et al. (2020). With a low rate of star formation (Fig. A.1), Scl should have a top-light IMF (i.e., larger  $\alpha_3$ , cf. Lee et al. 2009). The IMF is also bottom-light (i.e., smaller  $\alpha_1$  and  $\alpha_2$ ) given the low stellar metallicities (Geha et al. 2013).

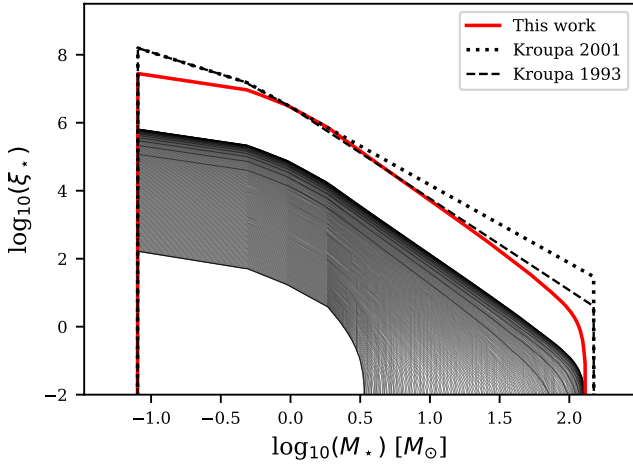


**Fig. A.2.** Time-integrated galaxy-wide IMF for all stars ever formed (thick solid red curve) and the galaxy-wide IMF for each 10 Myr star formation time step (thin solid curves) normalized by the total mass of a stellar population. Our best-fit IMF is compared with the canonical Kroupa (2001) IMF with  $\alpha_3 = 2.3$  (dotted line) and the solar-neighborhood IMF from Kroupa et al. (1993) with  $\alpha_3 = 2.7$  (dashed line).